et al. [12] intended to minimize the inter-institutional variation of images of Hoffman 3-dimensional phantom in a multicentre clinical study using PET devices supplied from different vendors.

The Hoffman 3-dimensional brain phantom is however limited attributed to its cylindrical outer structure rather than a realistic brain contour, and also to the bone or skull structure not being taken into account. These two factors are particularly important if one intends to apply it for evaluating SPECT images, because the attenuation coefficient map is usually estimated from the head contour by assuming a uniform attenuation coefficient value throughout the head object. Effects of errors in this process on errors in the reconstructed images could not be evaluated if the Hoffman 3-dimensional phantom is utilized. It is essential for the phantom to contain a fine 3-dimensional distribution of cerebral radioactivity with the skull and a realistic head contour.

This study was aimed at developing a 3-dimensional brain phantom that simulates a static cerebral blood flow distribution in the grey matter with an inclusion of the skull structure and a realistic head contour. A recently developed photo-curable laser-modelling technique with the lipophilic resin material was employed, so that the phantom contains liquid solutions for radioactivity and the bone-equivalent contrast agent. Attention was made in the construction procedures to avoid the supporting structures, so that the whole volume of the inner spaces of the phantom can be entirely filled with liquid. We also intended to establish the connectivity of liquid space so that air bubbles are to be removed. We then evaluated the feasibility of using this phantom in typical SPECT and PET imaging.

Materials and methods

Phantom design and construction

The phantom was made of a transparent photo-curable polymer, or polyepoxide with a density of 1.07 g/mL (TSR-829, CMET Inc., Yokohama City, Japan). This material has been optimized to improve its anti-water absorbing characteristics [13]. According to precise material elements, the database for the photon cross sections (XCOM) from the National Institute of Standards and Technology (http://physics.nist.gov/PhysRefData/Xcom/html/xcom1.html) estimated that the attenuation coefficients for 511, 159, and 140 keV were 0.101, 0.157, and 0.164 cm^{-1}, respectively. The phantom was constructed using a stereo-lithographic machine with the laser-modelling technique (model RM-6000, CMET Inc, Yokohama City, Japan), which can produce the 3-dimensional construction in 50 mμ resolution. It was intended not to include any supporting structures in the inner spaces. The manufacturing speed was decreased during the laser-beam construction, so as to ensure the solidity of the phantom, thus avoiding the possible distortion of the inner structure.

The procedures to construct the 3-dimensional phantom are illustrated in Fig. 1. The basic design of the phantom was first generated using a set of T1-weighted MR images of brain obtained from a healthy 26-year-old Japanese male volunteer. The specific sequence included the gradient echo with inversion recovery, which provided gap-less, tomographic images at 1.0-mm intervals. MR images were first segmented using a K-means procedure. Then, the head contour, skull regions, ventricular regions, tracheal air space, and grey and white matter segments were manually illustrated on the computer screen, in a 2-dimensional tomographic domain (Fig. 1a). The grey matter segment included the frontal, parietal, posterior, and temporal cortex areas with the striatum, thalamus, and mid-brain regions. The image size was 440 × 440 pixels (0.5 mm/pixel), and 51 slices were acquired at 3.6-mm axial slice intervals over the whole phantom. The grey matter structure was covered in 34 total slices. During the illustration procedure, a modification was made to remove global distortions in the head and brain structures and to fit a 3-dimensional head model. The tomographic data were then exported to a 3-dimensional computer-aided design (CAD) software (Rapidform2006-sp1, INUS Technology Inc., Seoul, South Korea). The volumetric data were then interpolated in the axial direction (see Fig. 1b). The grey matter and bone compartments were designed so that they could be filled with liquid solutions, and the remaining area, except for the tracheal space, was filled with a polymer resin (see Fig. 2). The grey matter component can be filled with a radioactive solution, and the skull region is typically filled with a bone-equivalent solution of K_2HPO_4 as suggested in an earlier study [14]. The white matter region was not to be filled with liquid but was made of a photo-curable polymer, and thus the white matter region became identical to the CSF and scalp. An attention was made to avoid closed areas in the grey matter and bone segments, so that every part of the compartments could be filled with liquid. The radioactive liquid and K_2HPO_4 solution can then be diluted into each of the two compartments. In addition, no supporting resin materials were placed both in the grey matter and skull components, although the standard procedure is to place fine pillars to support the fine structure particularly for horizontal wall. The speed of the stereo-lithographic manufacturing process was slowed down, with increased pitch (Fig. 1c). The manufacturing process required whole 3 days to complete. In total, five sets of phantoms were constructed. Of these, two sets were constructed at the same time from the first lot, while the other three were generated from the second lot.

Evaluation of the phantom

The weight and height of the phantom, as well as volumes of the grey matter and skull compartments were measured for all 5 phantoms. The phantoms were then scanned by X-ray CT using a Symbia T6 CT/SPECT hybrid scanner (Siemens, Chicago, IL, USA) without filling the phantom with liquid. The pixel size of the X-ray CT was $0.5 \times 0.5\ \text{mm}^2$, and the slice pitch was 1.5 mm. The agreement between the X-ray CT and digital design, and the consistency across the five phantoms were evaluated. Additional intention was whether the wall inside the phantom is smoothly constructed or not. Distilled water was mixed with a small amount of detergent and the grey matter compartment of a phantom was filled with it. The skull compartment was filled with the K_2HPO_4 solution at the suggested concentration [14]. Both compartments were scanned again using X-ray CT. The X-ray CT images were investigated whether air bubbles remained in the phantom or not.

A transmission scan was carried out on these phantoms using a 3-headed gamma camera (Toshiba GCA-9300, Tokyo, Japan) fitted with 400-mm focal length, low energy, high resolution, symmetric fan beam collimators (N2) from the same vendor. The procedures have been described in our earlier protocol [2, 15, 16] and were shown to provide an accurate attenuation μ map of the object [2, 15, 16]. The 132-mm rotation radius used in these studies resulted in a reconstructed field of view (FOV) with a 22-cm diameter

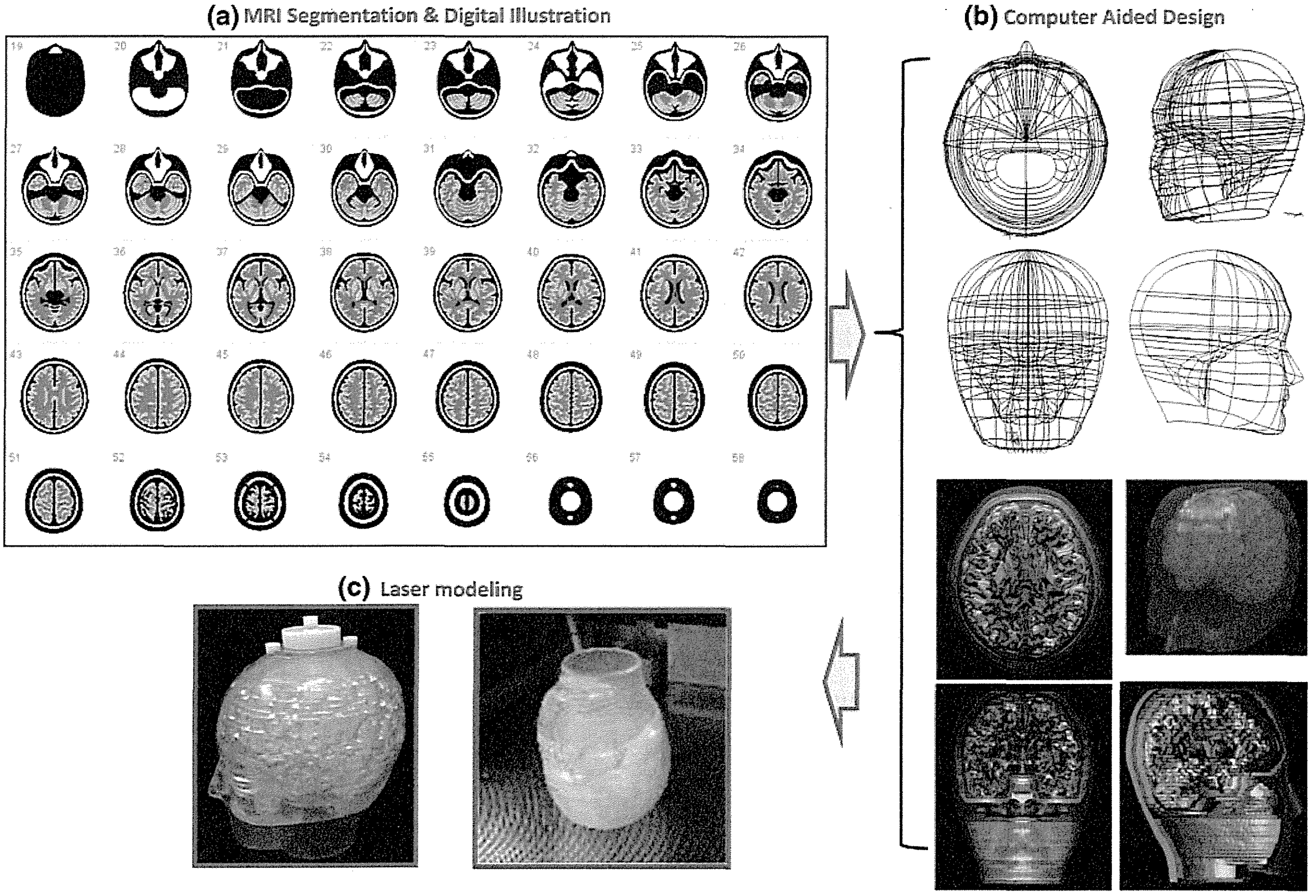

Fig. 1 Illustrative procedures to develop the 3-dimensional brain phantom. **a** Tomographic images including the cortical grey matter, deep grey matter, white matter, cerebral spinal fluid space, skull, scalp and trachea regions that were generated at 3.6-mm intervals from anatomical MR images of a young healthy volunteer. Data were manually modified to fit to a head model. **b** Three-dimensional data were then generated using the computer-aided-design software, and modifications were made to guarantee the connectivity of both the grey matter and bone compartments. Careful attention was made to establish a liquid flow stream within the structure so that air bubbles could be easily removed from the liquid space. **c** A laser-modelling technique with a stereo-lithographic machine and a photo-curable material was employed to construct the 3-dimensional phantom. There was special attention to avoid contamination from the resin-based supporting material inside the grey matter and skull compartments, and also to make the inner wall surface of the phantom as smooth as possible. The speed and pitch of the machine as well as the temperature and humidity were optimized

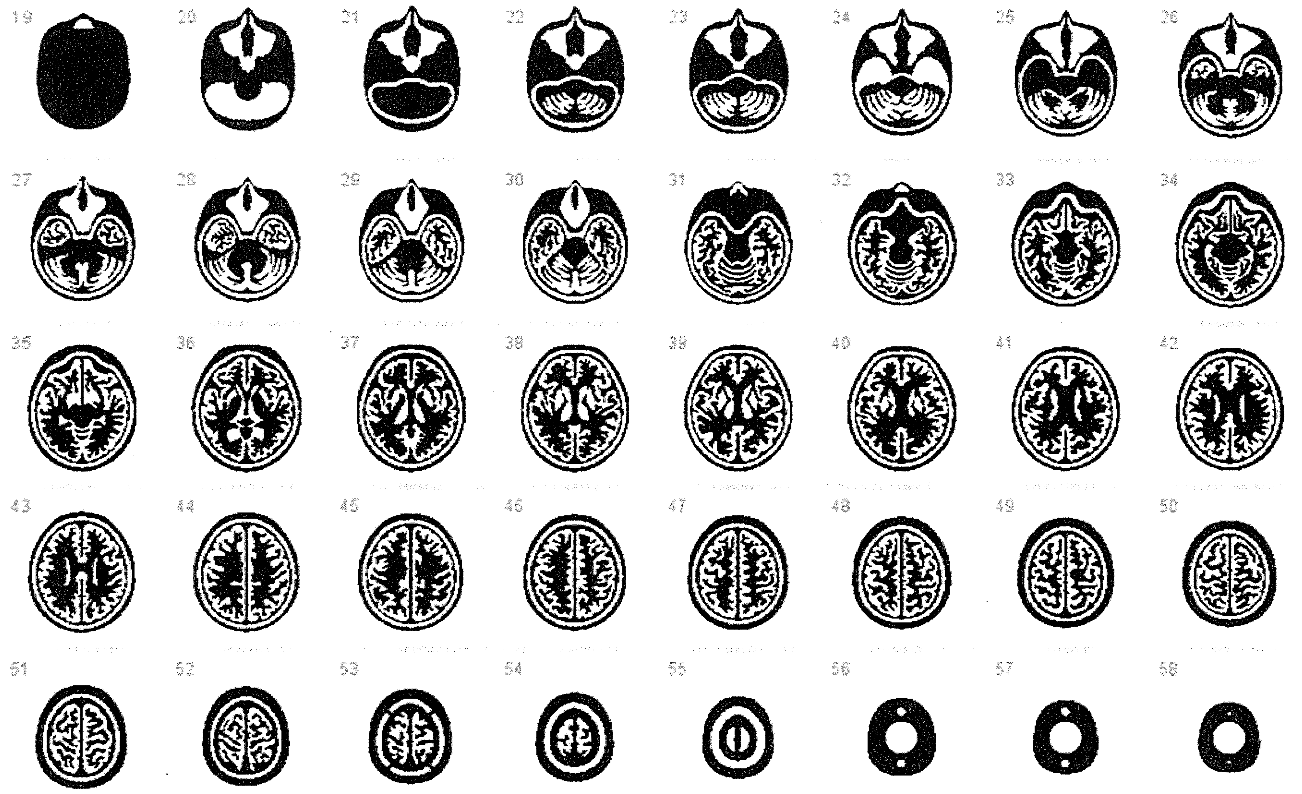

Fig. 2 Digital design of the phantom on a 2-dimensional domain. The *areas in white* correspond to the air space, which may be filled with the radioactive solution and K_2HPO_4 solution for the grey matter and skull compartments, respectively. The additional air space corresponds to the trachea

[15]. One head was used for the transmission scan, and a 25-cm long ^{99m}Tc rod source (74 MBq) was placed at the focal line of its collimator. After a 15-min blank scan, transmission projection data were collected for 15 min. The SPECT cameras were continuously rotated to collect 90 projections over 360° (10 s/projection). The energy window selected was 20 % on 140 keV. After compensating for the radioactive decay of the ^{99m}Tc, the inverse of the projection data was multiplied by the blank projection data, to which the filtered-back projection program was applied to reconstruct images of the attenuation coefficients.

SPECT/PET acquisition

Two sets of SPECT scans were performed on a phantom using a Symbia T6 scanner from Siemens (Chicago, IL, USA) fitted with a low-energy high-resolution (LEHR) collimator set. In the first experiment, the grey matter compartment was filled with a ^{99m}Tc solution of approximately 20 MBq, while in the second experiment this compartment was filled with an ^{123}I solution of approximately 20 MBq. In both experiments, the skull region was filled with the K_2HPO_4 solution at the concentration suggested by de Dreuille et al. [14] (100 g of K_2HPO_4 diluted to 67 g of distilled water). The SPECT acquisition followed a standardized protocol for clinical CBF quantitation using ^{123}I-iodoamphetamine, as recently described [17]. Seven frames of a dynamic SPECT scan were acquired over a 28-min period at 4 min per frame. The matrix size was 64 × 64, and the number of projection data was 90. Before the reconstruction, all projection data were summed over the whole period, normalized for detector non-uniformity, and calibrated for the centre-of-rotation using the standard vendor software. Then, these data were reconstructed using the QSPECT reconstruction program, including the attenuation correction and scatter correction procedures, as recently described by Iida et al. [17]. A single threshold level (% of the peak of projection data), which was consistent with that in a clinical study, was assigned to define the head contour and generate a uniform attenuation coefficient map. Reconstructed SPECT images were calibrated in Bq/mL, which provides independence from the scanning parameters such as the acquisition time, number of views, matrix size, zoom factor, etc. [17].

Scans were also performed on a phantom using a ECAT ACCEL PET scanner (Siemens-CTI, Knoxville, TN, USA), which provides an intrinsic spatial resolution of 4.5 mm full-width at half-maximum (FWHM) at the centre of the field-of-view (FOV). PET scanning was performed in 2-D mode. Following a 10-min transmission scan using a rotating external ^{68}Ge-^{68}Ga rod source, 18F-solution of approximately 37 MBq was inserted into the grey matter compartment of the phantom. PET scan was carried out for 10 min. Images were reconstructed using a standard Filtered-Back Projection (FBP) using a Hunning Filter, with standard correction procedures for random, detector normalization, attenuation, and scatter. Eight-millimetre post-filter also applied.

Data analysis

X-ray CT and SPECT images were registered to the digital design images of the phantom. The agreement with the X-ray CT images was visually analyzed for all five phantoms, particularly the agreement of fine structures of the cortex regions, the presence of residual resin materials in grey matter and bone compartments, and smoothness of the inner phantom surface or local distortion. It was also analyzed whether air bubbles were left in the grey matter or bone compartments on for the experiments filling both compartments with liquid.

Digital design images for the grey matter were extracted and were smoothed using a 3-dimensional Gaussian filter so as to match the spatial resolution of each of SPECT and PET images. The agreement between the SPECT and PET images acquired with the ^{99m}Tc and ^{123}I, and ^{18}F solutions; the digital design images were visually evaluated.

Three ROIs were placed on the attenuation coefficient images obtained from the ^{99m}Tc rod source-based transmission scan, namely the brain region, skull region, and whole head contour as carried out in our earlier study on young healthy volunteers [2, 15, 16]. The averaged attenuation coefficient values were obtained for each of these three ROIs and were compared with the values obtained for the young healthy subjects.

All data are presented as the mean ± 1 SD. Student's t test was used to evaluate the difference, and $p < 0.05$ was considered statistically significant.

Results

The results from the phantom assessment are summarized in Table 1. The volume of the skull component was 306.0 ± 1.9 mL, which was consistent with the expected volume of this component calculated as a summation of the surface area at each slice times the slice interval (305.6 mL). However, the grey matter volume was 562.2 ± 0.9 mL, which is 11.6 mL (2.1 %) greater than the estimated value of 550.6 mL. The phantom height was 212.7 ± 0.1 mm, and the weight of the phantom, excluding the internal liquid, was 1996.8 ± 1.9 g. It is important to note that once the phantom was filled with water, the weight becomes heavier than the original weight. It required more than a day to remove water inside the compartments so that the weight becomes closer to the original value <5 g.

Figure 3a, b shows example X-ray CT images of a phantom without and with filling liquid into the compartments, respectively. Both images were aligned and re-sliced to match to the digital design images shown in Fig. 2. Note that X-ray CT images demonstrated a high contrast in the bone area due to K_2HPO_4 solution, and slightly reduced contrast in the grey matter area compared to the polymer resin areas. The visual analysis showed no particular distortion of the fine structure or resin materials remaining inside the compartments, as were also in other 4 phantoms. It was also confirmed that there were no apparent differences among the five phantoms on the X-ray CT images. No air bubbles were visible in either component.

The results of the attenuation coefficient values measured by the transmission scan using a SPECT camera are summarized in Table 2, along with values observed in healthy young volunteers in a previous study using the same procedures [2]. The attenuation values observed were 0.168 ± 0.006, 0.161 ± 0.006 and 0.206 ± 0.008 cm^{-1}, corresponding to the value averaged over the whole head contour at the slice indicating the maximum cross section, the cortical grey matter region and the skull (bone) region,

Table 1 Physical assessment of five pieces of the 3-dimensional brain phantom. The volume of the bone space essentially agreed with the designed parameter, but the grey matter region had a significantly greater value by 11.6 mL (2.1 %)

	#Phantom	Grey vol (mL)	Bone vol (mL)	Weight (g)	Height (mm)
1	1	564	303	1999	212.80
1	2	562	307	1996	212.80
2	3	563	308	1994	212.62
2	4	562	306	1998	212.69
2	5	562	306	1997	212.67
	Mean ± SD	562.6 ± 0.9	306.0 ± 1.9	1996.8 ± 1.9	212.7 ± 0.1
	Ideal value	550.6 mL	305.6 mL		

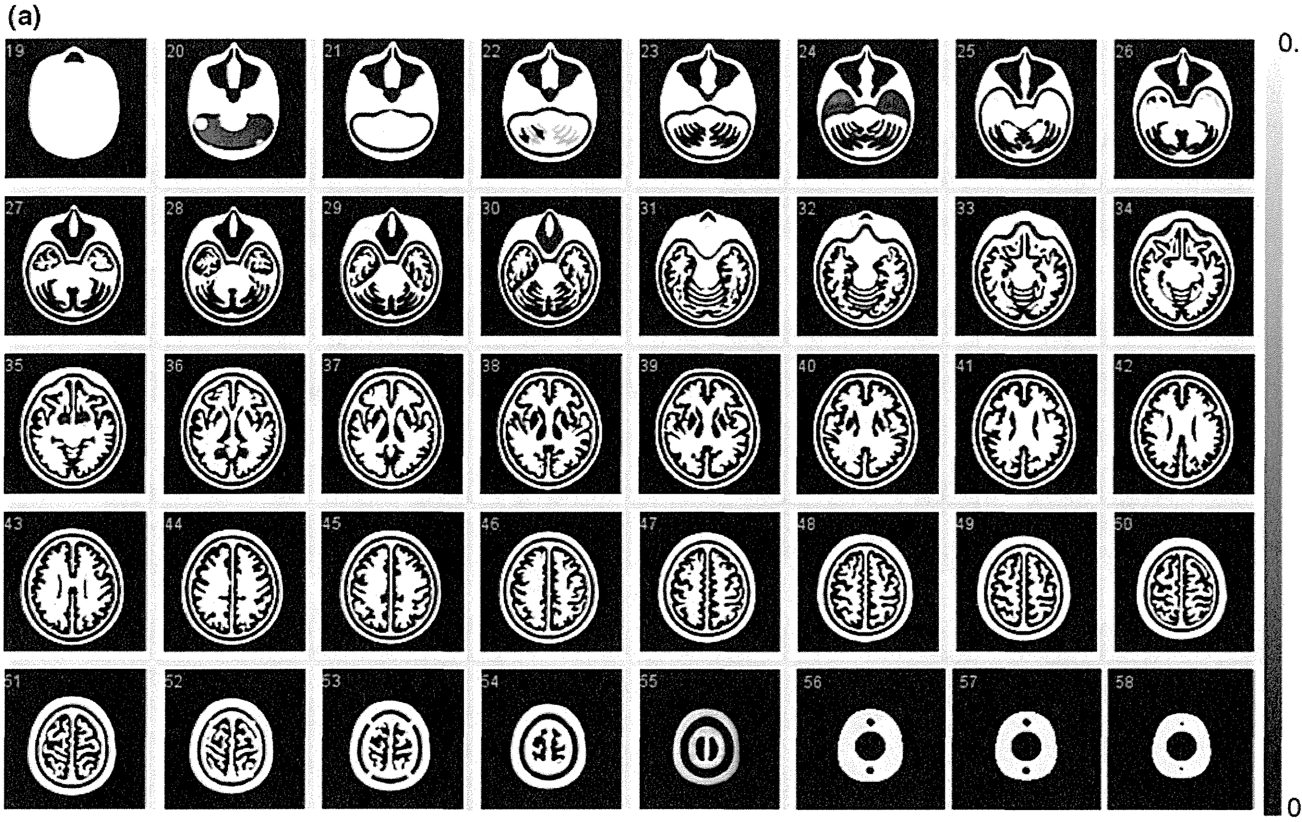

Fig. 3 **a** X-ray CT image of the developed phantom, which does not contain water or bone-equivalent liquid inside the phantom. Note that the images are converted to attenuation μ value with a peak value of 0.10 (cm^{-1}). The images are aligned to the digital design shown in Fig. 2. No remaining materials or irregular surface are seen inside the grey matter or bone compartments of the phantom. **b** X-ray CT images of a phantom that contains water in the grey matter region, and a K_2HPO_4 solution in the bone compartment. Note that the images are converted to attenuation μ value with a peak value of 0.20 (cm^{-1}). The images are aligned to the digital design of Fig. 2. There are no air bubbles remaining in the phantom

respectively. These values were similar to those from the healthy volunteers determined by the same criteria in our earlier study, which were 0.166 ± 0.01, 0.155 ± 0.007 and 0.197 ± 0010 cm^{-1}, respectively.

Figure 4 shows simulated images of the phantom, which represent only the grey matter component, without and with a 3-dimensional Gaussian filter that corresponded to the spatial resolution of the reconstructed SPECT images. Although homogeneous counts are assumed over the entire grey matter regions, the smoothed images (16 mm FWHM) represent inhomogeneous distribution. Figure 5 shows reconstructed SPECT images of the phantom, in which the grey matter component was filled with the ^{99m}Tc and ^{123}I solution, and the bone compartment was filled with the K_2HPO_4 liquid. The images, reconstructed using the QSPECT software including the attenuation, scatter correction using the attenuation coefficient images generated by means of the edge detection on the SPECT image, demonstrated reasonable agreement with the simulated images shown in Fig. 4 for both ^{99m}Tc and ^{123}I. Detailed structure is identical including the left–right asymmetrical distribution as follows; the counts in the occipital lob region as indicated in (a) are attributed to the thicker structure of the grey matter in this region, and the small spots indicated by (a–d) arrows are attributed to the presence of the cortical fissure. Images were also similar between the ^{99m}Tc and ^{123}I images.

Results from PET experiments are also compared with the simulated digital images in Fig. 6. Images showed good agreement with the digital design after smoothing with a Gaussian filter of 9 mm FWHM.

Figure 7 demonstrates the effects of applying a different magnitude of 3-dimensional Gaussian filter to the simulated phantom images that contain radioactivity only in the grey matter compartment. A greater amount of smoothing filter resulted in a reduced high-to-low contrast of the phantom images. Note that a particular part of the structure vanishes, and other regions become a cluster, by increasing the FWHM. It can be seen that relative contrasts in the phantom images vary dependent on the magnitude of 3-dimensional smoothing factor, largely attributed to the grey matter structure on the 3-dimensional domain.

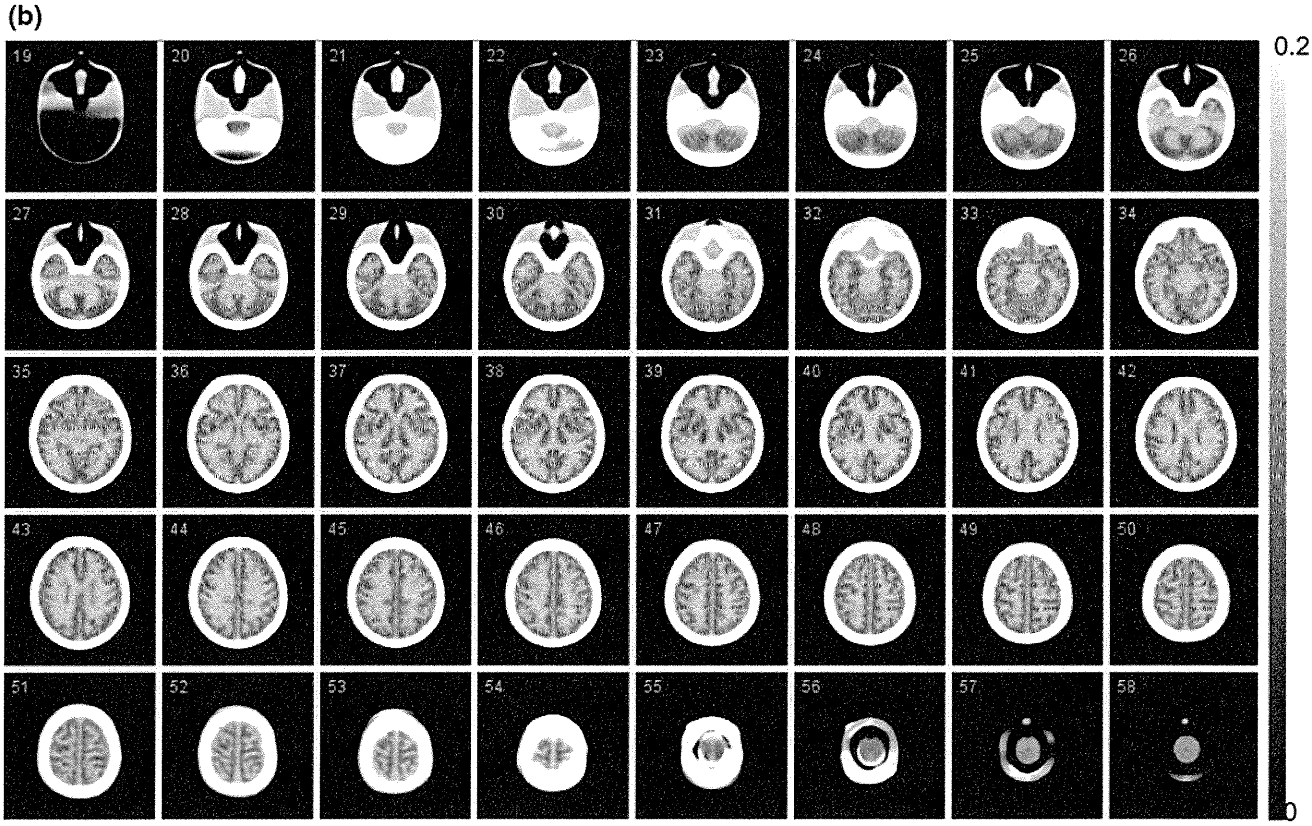

Fig. 3 continued

Table 2 Results of attenuation μ values for the averaged brain, cerebral region, and bone region that were obtained with the ^{99m}Tc-based transmission assessment

	μ values (cm^{-1})	
	Phantom	Human
Averaged over head	0.168 ± 0.006	0.166 ± 0.010
Cerebral tissue	0.161 ± 0.006	0.155 ± 0.007
Bone	0.206 ± 0.008	0.197 ± 0010

Discussion

This study demonstrated that the photo-curable laser-modelling technique, using the hydrophobic resin, can be used to construct a 3-dimensional brain phantom containing a fine grey matter structure with a detailed head contour and skull-equivalent and trachea components. With careful attention during the manufacturing process, the constructed phantoms appeared to be reasonably reproducible and agreed with the digital design within the accuracy of our image-registration technique. The supporting structures in the inner spaces, which have been the need in typical manufacturing process, could have been well avoided, providing smooth, non-distorted structure inside the grey-matter and skull compartments. The optimized procedures, including the decreased manufacturing speed during the laser-beam construction, pitch selection, and temperature, appeared to be adequate to ensure the solidity and reproducibility of the phantom.

As shown in Table 1, the variation in the volumes was ±0.2 % (or 0.9 mL) and ±0.6 % (or 1.9 mL), corresponding to the grey matter and skull regions, respectively. The total weight and height were also reproducible with variations of ±0.1 % and ±0.05 %, respectively. The attenuation coefficients of the phantom (Table 2), which were obtained using a ^{99m}Tc-rod source transmission measurement, were equivalent to those in healthy volunteers, which were assessed using the same experimental procedures in our earlier study for the whole brain, the cerebral tissue area, and the skull area [2]. This is because the photo-curable material used in this study has a similar attenuation coefficient and density (1.07 g/mL) compared to those of the human brain. The X-ray CT images shown in Fig. 3a, b demonstrated a good agreement with the digital design of the phantom shown in Fig. 2. More importantly, there were no residual resin materials on the X-ray CT images, nor any irregular inner wall surface of the phantom in the grey matter or bone compartments. The photo-curable laser-modelling technique usually requires supporting bridges (or pillar structures) when designing

Digital data

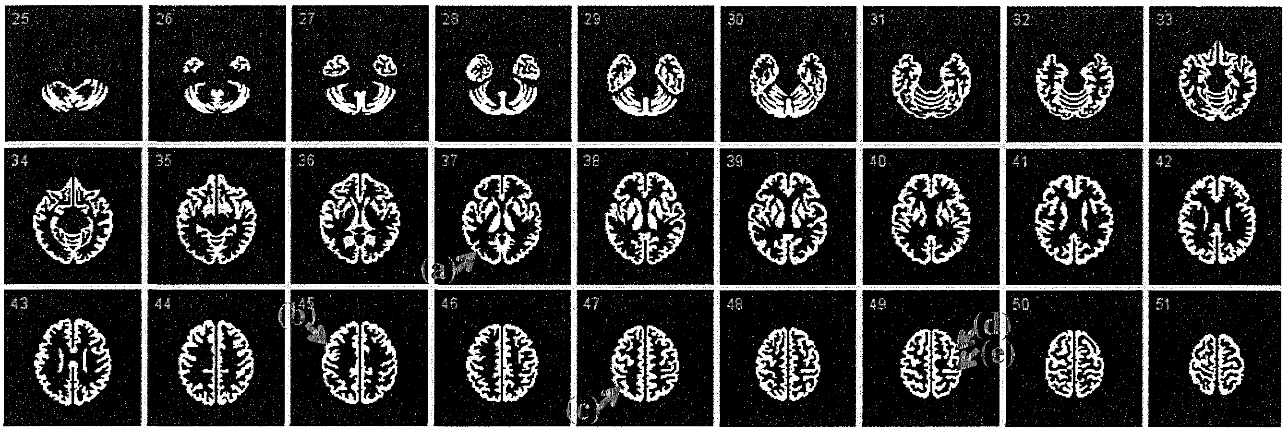

Digital data smoothed with a Gaussian filter (16 mm FWHM)

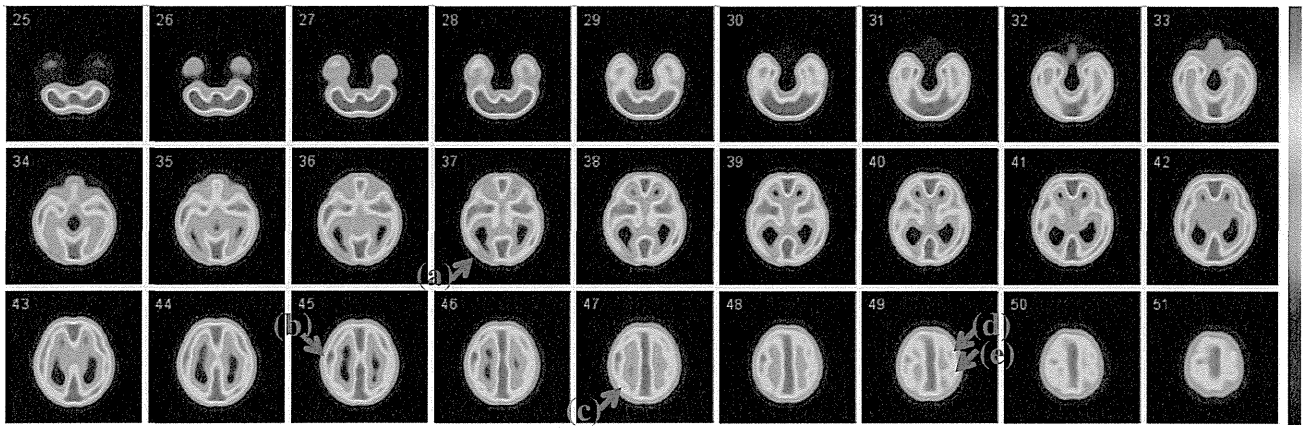

Fig. 4 Digital design of the grey matter area of the phantom in the original form (*top*) and after a smoothing operation with a Gaussian Filter of 16-mm full-width at half maximum (*bottom*), which corresponds to the spatial resolution of the SPECT images shown in Fig. 7. Note that the digital design data are noted with unity and null values, corresponding to the grey matter and other regions, respectively

structures in the horizontal direction. Our efforts of choosing optimal manufacturing procedures including the reduced speed, temperature and pitch, appeared to be feasible in order to remove such a supporting structure, which is essential in this 3-dimensional brain phantom. It is also important to note that the air bubbles could be well removed relatively easily from both the grey matter and bone compartments due to the connectivity of the liquid space.

In this phantom, we used a bone-equivalent solution of K_2HPO_4 as suggested in an earlier study [14]. This solution is known to have similar photon absorption coefficient values with bone or hydroxylapatite for a wide photon energy range, e.g., from 60 to 600 keV. This enables the applicability of this phantom even to the X-ray CT-based attenuation correction assessment. Use of this phantom also for PET acquisition with the energy of 511 keV is also valid. It should be noted that K_2HPO_4 is water soluble, and the solution could be concentrated until absorption coefficient values become greater than that of the human bone, while hydroxyapatite is not water-soluble. The water-soluble attenuation material is advantageous.

Of the note is that the SPECT images of the 3-dimensional brain phantom were consistent with the digital design of the phantom for both ^{99m}Tc and ^{123}I, after applying a Gaussian filter that corresponded to the spatial resolution of the reconstructed images. This is attributed to the accurate reconstruction software (QSPECT) [2, 17], including adequate attenuation- and scatter-correction procedures, employed in this study [2, 17]. The identical images between the ^{99m}Tc and ^{123}I isotopes further suggest the adequacy of the compensation procedures for penetration from high-energy photons emitted from the ^{123}I isotope itself [2, 17]. PET images reconstructed with the standard FBP procedures including the detector normalization, random, attenuation, and scatter correction processes were in a good agreement with the smoothed digital design images.

(a) Tc-99m

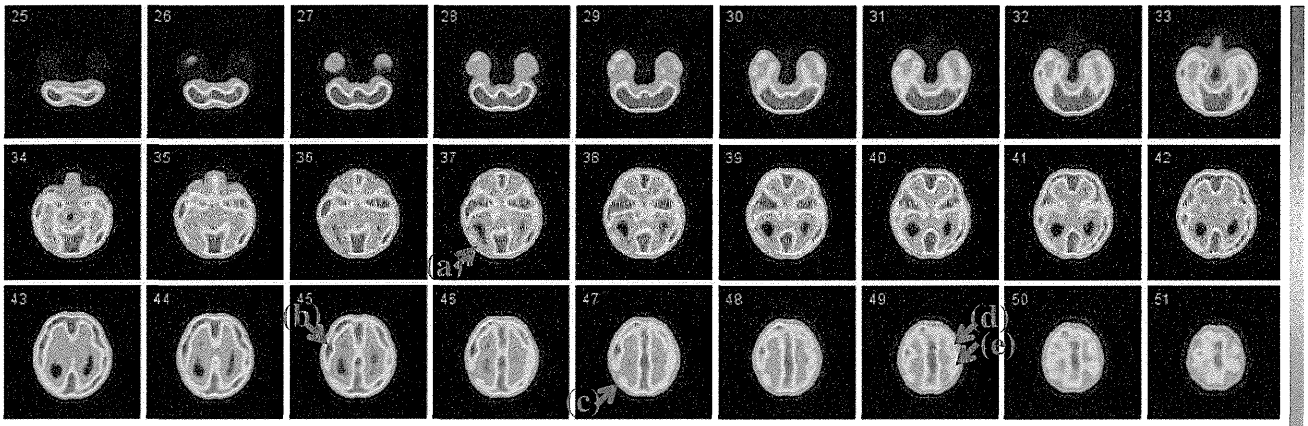

(b) I-123

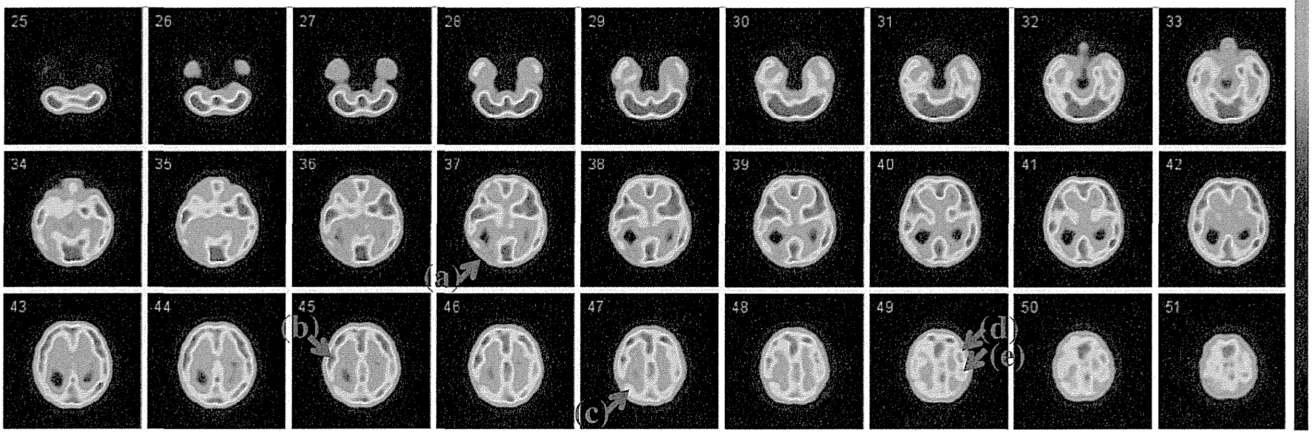

Fig. 5 SPECT images of the phantom filled with a ^{99m}Tc solution (*top*) and ^{123}I solution (*bottom*) in the grey matter compartment and a K_2HPO_4 solution in the bone compartment. Both images are aligned to the digital design shown in Fig. 4. SPECT images of the phantom filled with a ^{99m}Tc solution (*top*) and ^{123}I solution (*bottom*) in the grey matter compartment and a K_2HPO_4 solution in the bone compartment. Both images are aligned to the digital design shown in Fig. 4

This phantom may help evaluating the quality of clinical PET and SPECT brain images assessed with a variety of equipment installed at different institutions. There are several error factors that may cause distortion or irregular radioactivity distribution in the reconstructed images, attributed to imperfect attenuation- or scatter-correction procedures and/or other physical error sources. Quantitatively assessing these factors are often important in multicenter-clinical trials using existing SPECT and PET devices. Recently, Joshi et al. [12] proposed to assess the cross-consistency of PET images from different institutions using the Hoffman 3-dimensional brain phantom. The 3-dimensional brain phantom presented in this article may be better suited for such purpose. Joshi et al. [12] demonstrated that errors introduced by the attenuation and scatter correction procedures are significant and vary depending on the PET device. They also demonstrated that these errors are very different for human brain as compared with those for the Hoffman 3D brain phantom, because of the cylindrical shape of the Hoffman brain phantom with no skull or neck in the Hoffman 3D brain phantom. The phantom developed in this study might be better suited for determination of the attenuation and scatter correction errors for PET in multicentre studies. Further, advantage of the present phantom could be in the usage of evaluating brain SPECT images. Brain SPECT reconstruction often employs a software-based head contour detection for generating an attenuation coefficient distribution, as also done in QSPECT software. The present phantom is suitable in order to evaluate adequacy of the head-contour detection algorithm. Additional error factor could be due to the contribution of radioactivity outside of FOV. This might be evaluated by placing additional radioactivity source that simulates the clinical distribution for each radiotracer. Further systematic studies would be needed in order to confirm the real contribution in multicenter studies using SPECT.

Digital design data with Gauss Filter (9 mm FWHM)

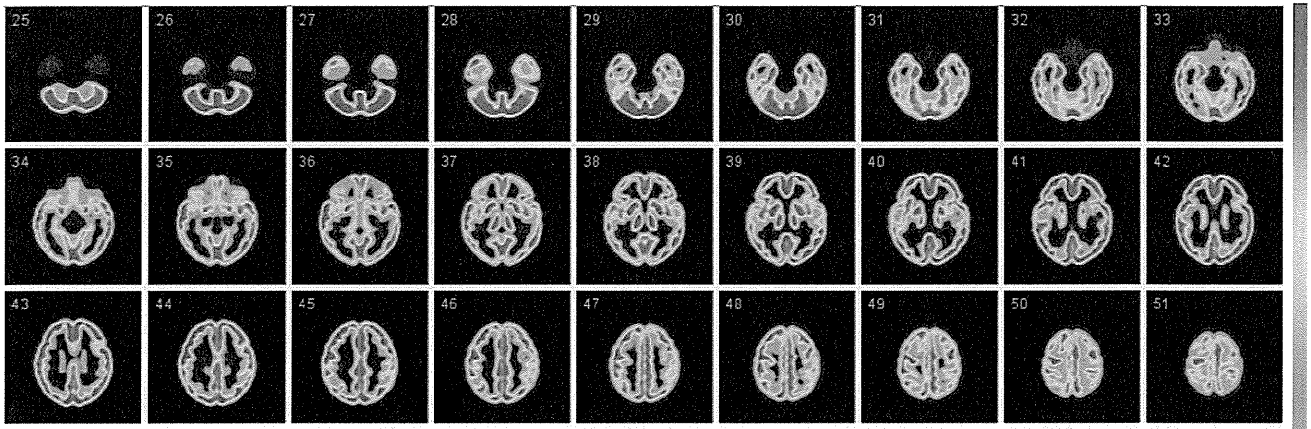

3D Brain Phantom measured with ACCEL PET scanner (2D mode)

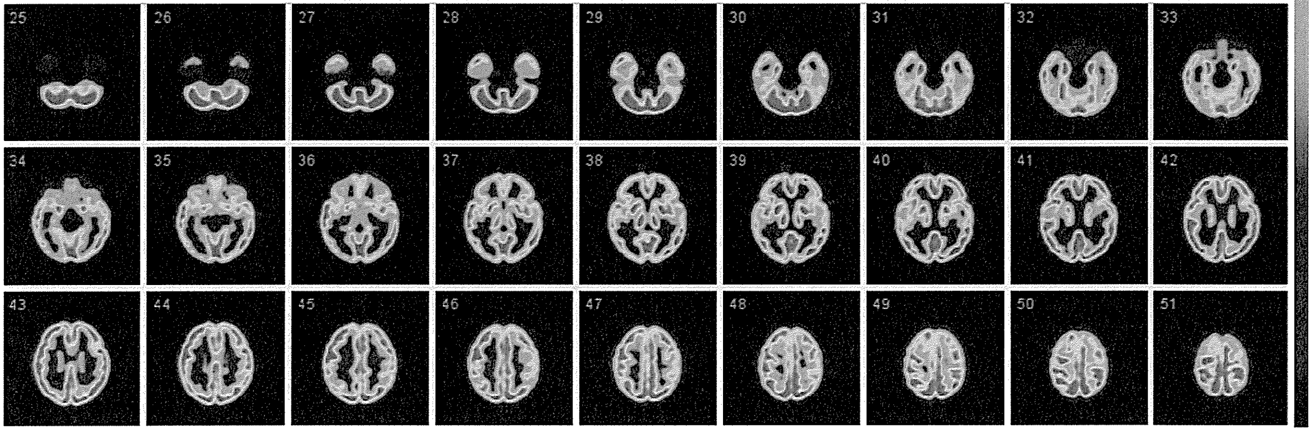

Fig. 6 Digital design of the grey matter area of the phantom after a smoothing operation with a Gaussian Filter of 9-mm full-width at half maximum (*top*), and PET images of the phantom filled with a ^{18}F solution (*bottom*). PET images are aligned to the digital design shown on *top*

The photo-curable polymer has been known to absorb water into the polymer materials and thus could alter the volumes. However, a recently developed water-repellent epoxy-resin (TSR-829) [13] seemed to be an appropriate material for the phantom, as there was minimal dilution of the water-liquid into the resin. The persistence of water in the grey matter and bone compartments after removing the water-liquid is attributed to the surface tension of water. The total weight of the phantom could become the original value when removing the water from the phantom, after 1 day of dry. Although further careful investigations are needed, the results in the present study suggest that this phantom is an adequate tool to evaluate PET/SPECT image quality.

A systematic discrepancy of 11.6 mL (approximately 2 %) was observed in the grey matter volume compared to the digital design. This could have occurred during the axial interpolation in the CAD procedures. Note that the digital data are given as tomographic data at 3.6-mm intervals, and a 3-dimensional interpolation was done to establish the slice-to-slice connectivity. Therefore, the digital data are not necessarily identical to the actual structure of the constructed phantom. However, the difference was not clearly visible in the X-ray CT images compared with the digital design. Intrinsic differences should be present in the precise structure and volume of the constructed phantom, but the reproducibility of the phantom is probably a more important issue. Further investigation is needed.

One drawback of the present 3-dimensional brain phantom compared to the Hoffman 3-dimensional phantom is that there is no structure corresponding to the white matter region. It is theoretically possible to insert small structures in the white matter regions, but additional work will be required to establish a liquid flow in these regions. In addition, air bubbles may be difficult to be removed, requiring further technical challenges.

The reconstruction program used in this study was a QSPECT program and was recently evaluated in a multicenter study [17]. The study demonstrated the adequacy of quantitating cerebral blood flow images both at rest and after acetazolamide treatment in clinical institutions, but

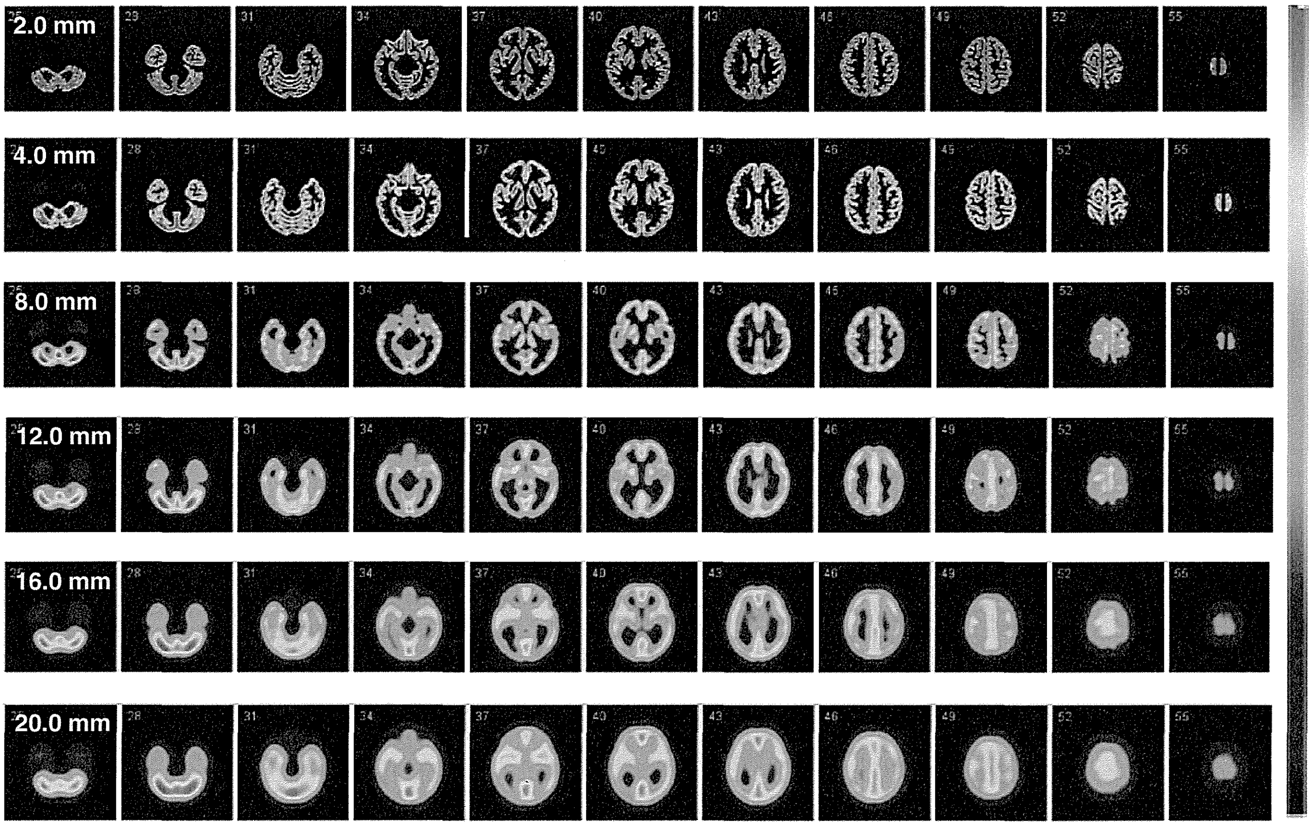

Fig. 7 Digital images of the grey matter region of the phantom with various magnitudes of the 3-dimensional Gaussian filter. The magnitude of the filter is given as full-width at half-maximum. Smoothing reduces the contrast, and the magnitude of modification varies at different regions, depending on the structure

further evaluations of the physical accuracy and cross-institutional consistency of reconstructed images are required among the participating institutions. The present 3-dimensional brain phantom might be valuable for this purpose, particularly when data are obtained with a variety of clinical settings and equipment. These studies are highly desired in the future.

A recent report also suggested the impact of utilizing the SPECT device in multicenter clinical trials. This is based on the physical features of the SPECT equipment, namely that the magnitude of the two major sources of attenuation and scatter errors is independent of the scanner in SPECT, unlike in PET. Scatter and attenuation occur in the object and are thus object dependent, but are not dependent on the geometry of the imaging equipment [18]. Therefore, once a software program is developed to provide accurate image reconstruction with compensation for both attenuation and scatter, the program should be able to provide quantitative images that are intrinsically independent of the geometric design of the SPECT cameras. This is an attractive feature of SPECT for multicenter clinical studies. The present 3-dimensional brain phantom would be valuable in order to verify this concept.

Conclusion

A 3-dimensional brain phantom containing the grey matter, skull, and tracheal structures with a realistic head contour has been developed using a laser-modelling technique with a photo-curable polymer (transparent TSR0829; 1.07 g/mL). The high consistency with digital data and reproducibility across constructions suggest that this phantom can be used for multicenter evaluations of PET and SPECT images.

Acknowledgments The authors would like to thank Ms. Kagari Takada from GK-Design Studio, Suita City, Japan, for help manipulating the 3-dimensional digital data. Thanks are also given to Mr. Shota Murakami from National Cerebral and Cardiovascular Center, Suita City, Japan for assistance with the data and software. The present study was supported by a Grant from the Ministry of Health, Labour and Welfare (MHLW) of Japan, and also partly by the Japan Cardiovascular Research Foundation, Suita City, Japan. No potential conflicts of interest were disclosed.

References

1. Iida H, Nakagawa J, Yamada S, Matsuda H, Maruno H, Nakajima T, et al. Image reconstruction in SPECT: standardization of image processing. Kaku Igaku. 2009;46:109–11.
2. Iida H, Narita Y, Kado H, Kashikura A, Sugawara S, Shoji Y, et al. Effects of scatter and attenuation correction on quantitative assessment of regional cerebral blood flow with SPECT. J Nucl Med. 1998;39:181–9.
3. Kemp BJ, Prato FS, Dean GW, Nicholson RL, Reese L. Correction for attenuation in technetium-99 m-HMPAO SPECT brain imaging. J Nucl Med. 1992;33:1875–80.
4. Kim KM, Varrone A, Watabe H, Shidahara M, Fujita M, Innis RB, et al. Contribution of scatter and attenuation compensation to SPECT images of nonuniformly distributed brain activities. J Nucl Med. 2003;44:512–9.
5. Stodilka RZ, Kemp BJ, Prato FS, Nicholson RL. Importance of bone attenuation in brain SPECT quantification. J Nucl Med. 1998;39:190–7.
6. Bloomfield PM, Spinks TJ, Reed J, Schnorr L, Westrip AM, Livieratos L, et al. The design and implementation of a motion correction scheme for neurological PET. Phys Med Biol. 2003;48:959–78.
7. Ter-Antonyan R, Jaszczak RJ, Greer KL, Bowsher JE, Metzler SD, Coleman RE. Combination of converging collimators for high-sensitivity brain SPECT. J Nucl Med. 2009;50:1548–56.
8. Woo S, Watabe H, Choi Y, Kim K, Park C, Bloomfield M, et al. Sinogram-based motion correction of pet images using optical tracking motion tracking system and list-mode data acquisition. IEEE Trans Nucl Sci. 2004;51:782–8.
9. Ardekani BA, Braun M, Hutton BF, Kanno I, Iida H. Minimum cross-entropy reconstruction of PET images using prior anatomical information. Phys Med Biol. 1996;41:2497–517.
10. Muller-Gartner HW, Links JM, Prince JL, Bryan RN, McVeigh E, Leal JP, et al. Measurement of radiotracer concentration in brain gray matter using positron emission tomography: MRI-based correction for partial volume effects. J Cereb Blood Flow Metab. 1992;12:571–83.
11. Hoffman EJ, Cutler PD, Digby WM. Mazziotta JC 3-D phantom to simulate cerebral blood flow and metabolic images for PET. IEEE Trans Nucl Sci. 1990;37:616–20.
12. Joshi A, Koeppe RA, Fessler JA. Reducing between scanner differences in multi-center PET studies. Neuroimage. 2009;46:154–9.
13. Hagiwara T. Recent progress of polymer materials for laser-modeling. Sokeizai. 2005;46:19–23.
14. de Dreuille O, Strijckmans V, Almeida P, Loc'h C, Bendriem B. Bone equivalent liquid solution to asses accuracy of transmission measurements in SPECT and PET. IEEE Trans Nucl Sci. 1997;44:1186–90.
15. Ichihara T, Motomura N, Ogawa K, Hasegawa H, Hashimoto J, Kubo A. Evaluation of SPET quantification of simultaneous emission and transmission imaging of the brain using a multi-detector SPET system with the TEW scatter compensation method and fan-beam collimation. Eur J Nucl Med. 1996;23:1292–9.
16. Iida H, Eberl S, Kim KM, Tamura Y, Ono Y, Nakazawa M, et al. Absolute quantitation of myocardial blood flow with ^{201}Tl and dynamic SPECT in canine: optimisation and validation of kinetic modelling. Eur J Nucl Med Mol Imaging. 2008;35:896–905.
17. Iida H, Nakagawara J, Hayashida K, Fukushima K, Watabe H, Koshino K, et al. Multicenter evaluation of a standardized protocol for rest and acetazolamide cerebral blood flow assessment using a quantitative SPECT reconstruction program and split-dose 123I-iodoamphetamine. J Nucl Med. 2010;51:1624–31.
18. Graham LS, Fahey FH, Madsen MT, van Aswegen A, Yester MV. Quantitation of SPECT performance: Report of Task Group 4, Nuclear Medicine Committee. Med Phys. 1995;22:401–9.

Nuclear Instruments and Methods in Physics Research A 702 (2013) 111–113

Contents lists available at SciVerse ScienceDirect

Nuclear Instruments and Methods in Physics Research A

journal homepage: www.elsevier.com/locate/nima

Verification of a semi-automated MRI-guided technique for non-invasive determination of the arterial input function in ^{15}O-labeled gaseous PET

Satoshi Iguchi [a], Yuki Hori [a], Tetsuaki Moriguchi [a], Naomi Morita [b], Akihide Yamamoto [a], Kazuhiro Koshino [a], Hidekazu Kawashima [a], Tsutomu Zeniya [a], Jun-ichiro Enmi [a], Hidehiro Iida [a,*]

[a] *Department of Investigative Radiology, National Cerebral and Cardiovascular Center Research Institute, 5-7-1, Fujishirodai, Suita, Osaka, 565-8565, Japan*
[b] *Department of Radiology, National Cerebral and Cardiovascular Center Hospital, 5-7-1, Fujishirodai, Suita, Osaka, 565-8565, Japan*

ARTICLE INFO

Available online 25 August 2012

Keywords:
Input function
Spillover correction
Partial volume effect
^{15}O PET

ABSTRACT

A semi-automated MR-guided technique has been evaluated for non-invasive estimation of cerebral metabolic rate of oxygen (CMRO$_2$) using the sequential administration of ^{15}O oxygen (O$_2$) and ^{15}O carbon dioxide (CO$_2$) during a single PET scan. Two mathematical models, which assess the arterial input function (AIF) from time-activity curves (TAC) in the internal carotid artery region, were tested, namely one with a simple correction for the recovery coefficient (RC) and another with corrections for RC and spillover from surrounding tissues. RC was determined from MRA and black-blood image. RC was also determined from C^{15}O blood volume images as a reference. RC agreed between MR-based and C^{15}O-PET based methods, suggesting validity of MR-based methods. Area-under-the-curve (AUC) of the early portion of estimated AIF agreed with that of measured AIF in both models. AUC of the delayed phase of estimated AIF was largely overestimated in the first model, but was sufficiently improved by the spillover correction implemented in the second model.

1. Introduction

PET study using ^{15}O gases (^{15}O$_2$, C^{15}O$_2$, C^{15}O, and H$_2^{15}$O) provides absolute quantification of cerebral blood flow (CBF), cerebral metabolic rate of oxygen (CMRO$_2$), oxygen extraction fraction (OEF), and cerebral blood volume (CBV). The continuous monitoring of the arterial radioactivity concentration using a small detector is prerequisite, but has been considered non-practical for a clinical use due to its invasiveness and the need for labor intensive work. Recent advances in PET devices enable quantitative assessment of time-activity curves (TAC) in the area of the internal carotid artery (ICA), by which arterial input functions (AIF) may be replaced. However, the small structure of the ICA causes systematic underestimation due to small recovery coefficient (RC) and spillover (SP) from the surrounding tissues [1]. Hybrid MR/PET has a potential providing the PET-derive AIF with accurate and reliable corrections for RC and SP using MR-based anatomical information.

This study was intended to develop a semi-automated technique to derive AIF for a series of ^{15}O-PET scans using MR images. Validity of the technique is tested in the series of PET scans performed on healthy volunteers. The impact of RC and SP corrections has also been evaluated.

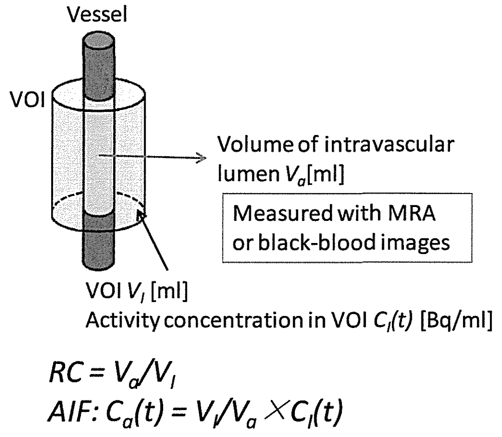

Fig. 1. Mathematical model for AIF estimation with a simple correction for the recovery coefficient (model-1).

Abbreviations: CBF, cerebral blood flow; CMRO$_2$, cerebral metabolic rate of oxygen; OEF, oxygen extraction fraction; CBV, cerebral blood volume; TAC, time-activity curve; ICA, internal carotid artery; AIF, arterial input function; RC, recovery coefficient; SP, spillover; VOI, volume-of-interest; DARG, dual-tracer autoradiographic method; TOF-MRA, time-of-flight magnetic resonance angiography; BB-FRFSE, black-blood fast recovery fast spin echo; AUC, area under the curve

[*] Corresponding author. Tel.: +81 6 6833 5012x2559; fax: +81 6 6835 5429.
E-mail address: iida@ri.ncvc.go.jp (H. Iida).

0168-9002/$ - see front matter © 2012 Elsevier B.V. All rights reserved.
http://dx.doi.org/10.1016/j.nima.2012.08.037

2. Method

2.1. Imaging protocol

Scans were carried out 9 times, on 7 healthy volunteers of 26+/−10 years old. The scanner was mCT from Siemens enabling 3D PET with adequate corrections for randoms, deadtime count loss, attenuation and scatter. Special attention was made in the scatter correction process to take into account for the strong radioactivity in gaseous form in the facemask. The scan protocol followed a recently proposed rapid dual-tracer autoradiographic method (DARG) [2,3], in which $^{15}O_2$ and $C^{15}O_2$ gases were inhaled sequentially within a 4.5 min interval, during a single PET scan over 9 min. A continuous arterial blood sampling was carried out, and AIF was assessed using a coincidence block detector, with adequate correction for delay and dispersion. Additional PET images were obtained with ^{15}O carbon monoxide (CO) inhalation to measure the RC of a volumes-of-interest (VOI) on ICA. Images were reconstructed at 5 sec interval, to which two VOIs were placed on the ICA region using semi-automated software. MR images were separately acquired on each volunteer with the sequence of 3D time-of-flight MR angiography (TOF-MRA) and 3D black-blood fast recovery fast spin echo (BB-FRFSE). The pixel size of the MR image was 0.6 × 0.8 × 1.0 mm^3 for TOF-MRA and 0.4 × 0.4 × 2.0 mm^3 for BB-FRFSE.

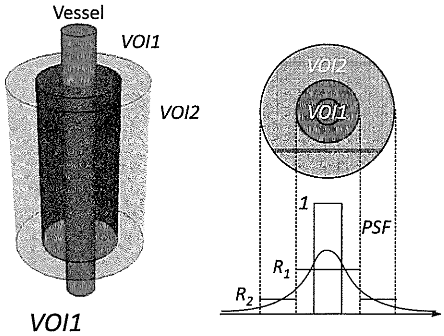

VOI1

$$C_1(t) = R_1 \times C_a(t) + (1 - R_1) \times C_t(t)$$

VOI2

$$C_2(t) = R_2 \times C_a(t) + (1 - R_2) \times C_t(t)$$

$C_1(t)$, $C_2(t)$: Activity concentration in VOI 1 and 2
R_1, R_2 : RC in VOI 1 and 2
$C_a(t)$: Radioactivity concentration in arterial blood
$C_t(t)$: Radioactivity concentration in surrounding tissue

Fig. 2. Mathematical model for AIF estimation with recovery coefficient and spillover correction (model-2).

Table 1
Comparison of AUC in the early phase of O_2 and CO_2 inhalation with a simple correction for the recovery coefficient.

	AUC ratio for O_2 (0–60 sec)			AUC ratio for CO_2 (0–60 sec)		
Subject	TOF-MRA	BB-FRFSE	CO	TOF-MRA	BB-FRFSE	CO
001-1	0.88	0.91	0.92	0.89	0.92	0.92
002-1	1.15	1.22	1.21	1.12	1.18	1.21
003-1	1.41	1.14	1.13	1.29	1.05	1.13
004-1	1.06	0.96	1.02	1.13	1.02	1.02
005-1	1.15	1.04	1.03	1.20	1.09	1.03
006-1	1.17	1.11	1.07	1.22	1.16	1.07
006-2	1.32	1.25	1.22	1.33	1.26	1.22
007-1	0.92	0.87	0.95	1.01	0.96	0.95
007-2	1.11	1.05	1.11	0.96	0.91	1.11
Mean	1.13	1.06	1.07	1.13	1.06	1.07
SD	0.17	0.13	0.11	0.15	0.12	0.11

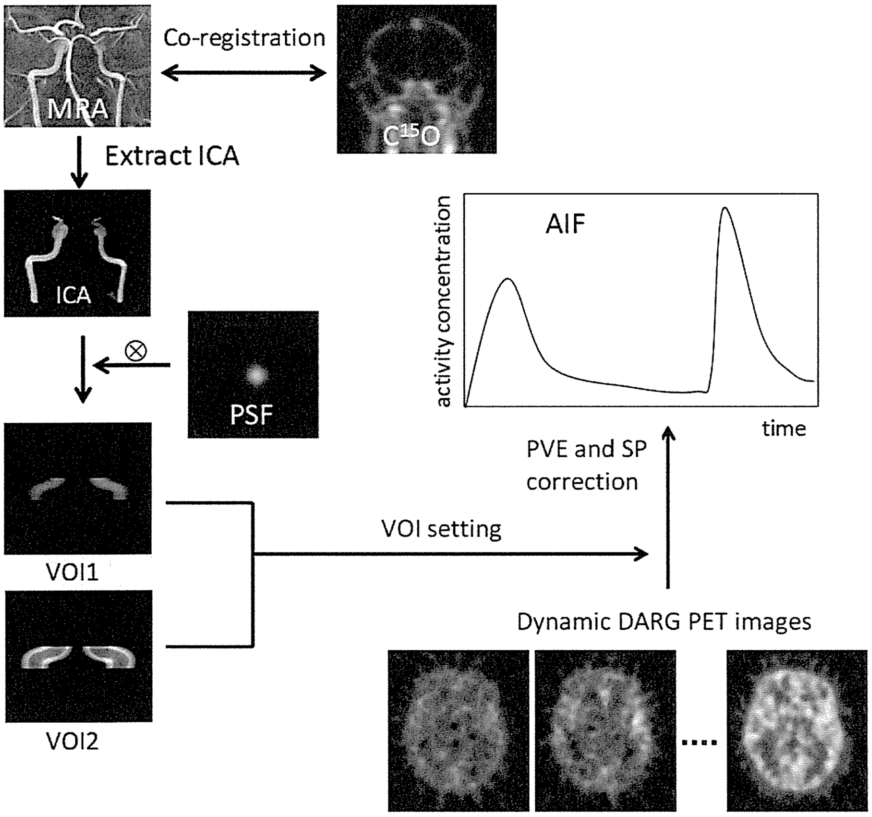

Fig. 3. Image processing for the AIF estimation by using semi-automated software. The process includes co-registration of MRI and PET images, automated extraction of ICA region, and calculation of AIF from dynamic PET images with RC and SP correction using two VOIs.

Table 2
Comparison of AUC in delayed phase of O_2 and CO_2 inhalation with a simple correction for the recovery coefficient.

	AUC ratio for O_2 (60–120 sec)			AUC ratio for CO_2 (60–120 sec)		
Subject	TOF-MRA	BB-FRFSE	CO	TOF-MRA	BB-FRFSE	CO
001-1	1.63	1.69	1.67	2.10	2.18	1.67
002-1	1.65	1.75	1.69	2.58	2.73	1.69
003-1	2.50	2.03	1.95	3.33	2.7	1.95
004-1	1.72	1.56	1.57	2.53	2.29	1.57
005-1	1.67	1.51	1.41	2.12	1.92	1.41
006-1	1.72	1.63	1.47	1.99	1.89	1.47
006-2	1.74	1.65	1.52	1.90	1.8	1.52
007-1	1.40	1.33	1.31	1.66	1.57	1.31
007-2	1.35	1.28	1.29	1.68	1.59	1.29
Mean	1.71	1.60	1.54	2.21	2.07	1.54
SD	0.33	0.22	0.21	0.53	0.43	0.21

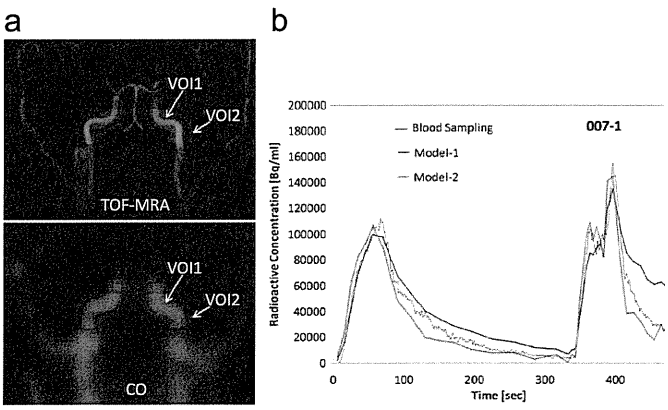

Fig. 4. a: Example of VOI setting fused on maximum projection images of TOF-MRA and CO PET data. VOI 1 and 2 were shown as red and blue region, respectively. b: Measured and estimated input functions in one subject. AIFs were estimated with the mathematical model-1 and model-2.

2.2. Model-1 (only RC correction)

To correct for the underestimation of the input function from ICA TAC, a mathematical model shown in Fig. 1 was applied to determine AIF with a correction for RC. The RC, which was defined as the volume of intravascular lumen-to-the volume of VOI ratio, was calculated using TOF-MRA and BB-FRFSE anatomical images, and was applied to ICA TAC to determine RC-corrected AIFs. RC was also determined from the $C^{15}O$ blood volume image in PET, and was applied to determine AIF.

2.3. Model-2 (RC and SP correction)

Correction for SP of radioactivity from surrounding tissues was taken into account, in addition to the RC correction described in the model-1. The mathematical model shown in Fig. 2 was used, and AIF was determined for given RC values for each of 2 VOIs. The process of image analysis for the AIF estimation using model-2 is shown in Fig. 3.

3. Results

The results of area under the curve (AUC) ratio for the three methods to determine RC for early portion (initial 60 sec) of $^{15}O_2$ and $C^{15}O_2$ scans obtained using the model-1 are summarized in Table 1. Similarly, the results for the delayed portion (60–120 sec) are summarized in Table 2. AIFs determined from ICA were 2.5–4.0 smaller than the measured AIFs. The simple correction for RC using TOF-MRA, BB-FRFSE, and CO images improved the agreement of AUC in the early part, but significantly overestimated in the delayed part.

Table 3
Comparison of AUC in early phase of O_2 and CO_2 inhalation with RC and SP correction.

	AUC ratio for O_2 (0–60 sec)		AUC ratio for CO_2 (0–60 sec)	
Subject	Model-1	Model-2	Model-1	Model-2
001-1	0.94	0.65	1.07	0.84
002-1	1.43	1.25	1.45	1.20
003-1	1.48	0.96	1.46	0.99
004-1	1.18	1.00	1.29	0.91
005-1	1.29	0.89	1.27	0.98
006-1	1.28	1.20	1.32	1.20
006-2	1.44	1.18	1.47	1.21
007-1	1.02	1.04	1.08	1.07
007-2	1.07	1.09	0.93	0.97
Mean	1.24	1.03	1.26	1.04
SD	0.20	0.18	0.20	0.14

Table 4
Comparison of AUC in delayed phase of O_2 and CO_2 inhalation with RC and SP correction.

	AUC ratio for O_2 (60–120 sec)		AUC ratio for CO_2 (60–120 sec)	
Subject	Model-1	Model-2	Model-1	Model-2
001-1	1.46	0.77	2.32	0.81
002-1	1.75	1.20	2.91	1.09
003-1	2.25	1.19	3.69	1.05
004-1	1.59	0.99	2.88	0.73
005-1	1.62	0.84	2.24	0.84
006-1	1.68	1.09	2.27	0.99
006-2	1.66	1.01	2.19	0.80
007-1	1.30	0.89	1.83	0.79
007-2	1.11	0.78	1.56	0.85
Mean	1.60	0.97	2.43	0.88
SD	0.32	0.17	0.64	0.13

Corrections for SP in addition to RC using the two VOIs (Fig. 4a) improved the agreement in AUC as compared with the invasive AIFs particularly for the delayed portion for both O_2 and CO_2 inhalation periods, as shown in Fig. 4b. The results of AUC comparison of model-1 and model-2 were summarized in Tables 3 and 4.

4. Conclusion

In the present study, we demonstrated the non-invasive MRI-guided AIF estimation from TAC in the ICA region in ^{15}O labeled gaseous PET. The AUC of the early phase of estimated AIF well agreed with that of measured AIF. On the other hand, The AUC of the delayed phase of estimated AIF was largely overestimated in model-1, and improved in model-2 by incorporating the SP correction with additional VOI placed surrounding area of the ICA.

These findings suggest that the combination of MR with ^{15}O gaseous PET enables a rapid and quantitative assessment of oxygen utilization simultaneously with the cerebral perfusion, providing unique opportunity for clinical research.

References

[1] P. Zanotti-Fregonara, E.M. Fadaili, R. Maroy, C. Comtat, A. Souloumiac, S. Jan, M.-J. Ribeiro, V. Gaura, A. Bar-Hen, R. Trebossen, Journal of Cerebral Blood Flow and Metabolism 29 (2009) 1825.

[2] N. Kudomi, T. Hayashi, N. Teramoto, H. Watabe, N. Kawachi, Y. Ohta, K.M. Kim, H. Iida, Journal of Cerebral Blood Flow and Metabolism 25 (2005) 1209.

[3] N. Kudomi, H. Watabe, T. Hayashi, H. Iida., Physics in Medicine and Biology 52 (2007) 1893.

Journal of Magnetic Resonance 229 (2013) 101–115

Contents lists available at SciVerse ScienceDirect

Journal of Magnetic Resonance

journal homepage: www.elsevier.com/locate/jmr

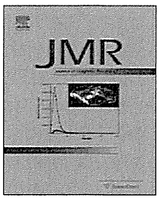

Advances in multimodal neuroimaging: Hybrid MR–PET and MR–PET–EEG at 3 T and 9.4 T

N. Jon Shah [a,b,*], Ana-Maria Oros-Peusquens [a], Jorge Arrubla [a], Ke Zhang [a], Tracy Warbrick [a], Jörg Mauler [a], Kaveh Vahedipour [a], Sandro Romanzetti [a], Jörg Felder [a], Avdo Celik [a], Elena Rota-Kops [a], Hidehiro Iida [d], Karl-Josef Langen [a], Hans Herzog [a], Irene Neuner [a,c]

[a] *Institute of Neuroscience and Medicine-4, Research Centre Jülich, 52425 Jülich, Germany*
[b] *Department of Neurology, Faculty of Medicine, JARA, RWTH Aachen University, Aachen, Germany*
[c] *Department of Psychiatry, Psychotherapy and Psychosomatics, RWTH Aachen University, Aachen, Germany*
[d] *Department of Investigative Radiology, National Cerebral and Cardiovascular Center Research Institute, 5-7-1, Fujishirodai, Suita, Osaka 565-8565, Japan*

ARTICLE INFO

Article history:
Received 30 September 2012
Revised 28 November 2012
Available online 10 December 2012

Keywords:
Ultra high-field MRI
Magnetic resonance imaging
Hybrid imaging
Multi-modal imaging
MR–PET
PET/MR
PET
Positron emission tomography
High resolution imaging
Metabolic imaging
Sodium imaging
EEG–fMRI
MR–PET–EEG

ABSTRACT

Multi-modal MR–PET–EEG data acquisition in simultaneous mode confers a number of advantages at 3 T and 9.4 T. The three modalities complement each other well; structural-functional imaging being the domain of MRI, molecular imaging with specific tracers is the strength of PET, and EEG provides a temporal dimension where the other two modalities are weak. The utility of hybrid MR–PET at 3 T in a clinical setting is presented and critically discussed. The potential problems and the putative gains to be accrued from hybrid imaging at 9.4 T, with examples from the human brain, are outlined. Steps on the road to 9.4 T multi-modal MR–PET–EEG are also illustrated. From an MR perspective, the potential for ultra-high resolution structural imaging is discussed and example images of the cerebellum with an isotropic resolution of 320 μm are presented, setting the stage for hybrid imaging at ultra-high field. Further, metabolic imaging is discussed and high-resolution images of the sodium distribution are presented. Examples of tumour imaging on a 3 T MR–PET system are presented and discussed. Finally, the perspectives for multi-modal imaging are discussed based on two on-going studies, the first comparing MR and PET methods for the measurement of perfusion and the second which looks at tumour delineation based on MRI contrasts but the knowledge of tumour extent is based on simultaneously acquired PET data.

1. Introduction

Tomographic imaging methodologies are essentially focused on the generation of tissue contrast in a given plane of interest. Contrast between different tissues arises from the differences in endogenous physical properties or through the introduction of exogenous “contrast agents”. Often a single contrast, or multiple contrasts from the same imaging modality, simply do not suffice to enable a complete diagnostic decision to be reached or, in scientific studies, leave aspects of the question unanswered. As such, a desire to address the same problem in different imaging machines arises. Specifically, spatial co-localisation of the information from the different modalities might be desired or indeed, the introduction of a temporal dimension might be required.

Magnetic resonance imaging (MRI) is characterised by its excellent tissue contrast based on, for example, T_1 and T_2 relaxation times, proton density, and diffusion/flow properties. Due to this fact, it has been widely used for structural/diagnostic imaging in the clinic and also for functional brain imaging in neuroscientific research.

Positron emission tomography (PET) is a widely used and well-established tool for clinical tumour diagnostics and is the gold standard for metabolic imaging. In contrast to MRI, PET provides insights into physiological and pathophysiological processes, albeit at a comparatively low anatomical resolution. Consequently, as shown here in an example from brain tumour imaging (see below), PET can be seen as an outstanding complement to MRI with respect to its metabolic specificity and its ability to enable tumour differentiation and tumour extent mapping [1].

Recently, two major developments in the fields of MRI and PET have taken place. In the MRI domain, the field strength of scanners for human application has moved to the ultra-high field range of

---

* Corresponding author at: Institute of Neuroscience and Medicine-4, Research Centre Jülich, 52425 Jülich, Germany.
E-mail address: n.j.shah@fz-juelich.de (N.J. Shah).

1090-7807/$ - see front matter © 2012 Elsevier Inc. All rights reserved.
http://dx.doi.org/10.1016/j.jmr.2012.11.027

up to 9.4 T and even beyond. Ultra-high fields facilitate structural imaging with significantly higher spatial resolution, higher functional (BOLD) contrast [2], perhaps even at the level of columnar resolution, and enhanced image contrast [3]. Moreover, such ultra-high field MRI scanners open up the opportunity to perform non-proton MRI and spectroscopy with a reasonable, PET-like spatial resolution in the order of 3 mm isotropic [4–6].

Regarding the use of PET in the MRI environment, the use of photo multiplier tubes (PMTs), that are extremely sensitive to magnetic fields, has been abandoned in favour of avalanche photo diodes (APDs) that are field insensitive. The implementation of new detector technologies based on APDs has led to true hybrid MR–PET scanners, capable of simultaneous MRI and PET data acquisition and has thus negated the need to perform scans in two separate machines. These hybrid scanners have the advantage of measuring PET and MRI datasets that are intrinsically co-registered in time and space [7–9]. Furthermore, inclusion of a PET scanner inside an MRI system brings with it advantages for PET image reconstruction. Partial volume correction, attenuation and motion correction can be performed based on MRI images acquired simultaneously with the PET data. In particular, clinical applications and neuroscientific research will benefit from these recent developments in terms of opportunities for metabolic imaging, accurate receptor density mapping, and novel paradigms for brain function.

In the confines of this article, multimodal imaging is defined as the summation of information from different imaging modalities whereby it is noted that MRI could well be regarded as being inherently multimodal, given the plethora of contrast mechanisms that can be exploited to generate image contrast. The combination of MRI and PET will be discussed; the measurement of MRI and PET data in two separate scanners will not be addressed and attention will instead be focused on hybrid MR–PET scanners studying the human brain and that are capable of the acquisition of simultaneous datasets. Hybrid MR–PET data acquisition at 3 T and at 9.4 T in humans will be explored. Further, the additional introduction of a temporal dimension, in the form of electroencephalography (EEG), in hybrid mode, will also be presented and discussed. Multimodal imaging in the form of simultaneous MR–EEG, and the extension thereof to triple modality MR–PET–EEG will also be briefly presented; the rationale for triple modal imaging is presented in Fig. 1 in the form of "finger print" diagrams.

2. Hybrid MR–PET scanner construction

The prototype 3 T MR–PET scanner used to obtain the results described herein comprises a commercially-available 3 T Siemens Tim Trio MR system and a custom-built BrainPET insert designed especially for brain imaging (Siemens Healthcare, Erlangen, Germany). The 9.4 T hybrid is also a Siemens prototype system based around a magnet with a warm-bore diameter of 90 cm and a PET insert that is nearly identical to that of the 3 T scanner. The BrainPET insert (Fig. 2) is a compact cylinder (length of 72 cm and an outer diameter of 60 cm) consisting of 32 copper-shielded detector cassettes each with six detector modules. The diameter of the PET field-of-view is 31.4 cm and 19.2 cm in the axial direction. The front end of the detector module is a 12 × 12 matrix of individual lutetium oxyorthosilicate (LSO) crystals coupled to a 3 × 3 array of APDs thus rendering the detector insensitive to the magnetic field of the MR system. The small volume of the LSO crystals measuring $2.5 \times 2.5 \times 20\ \text{mm}^3$ leads to a central PET image resolution of about 3 mm [10]; this is one of the best spatial resolutions for

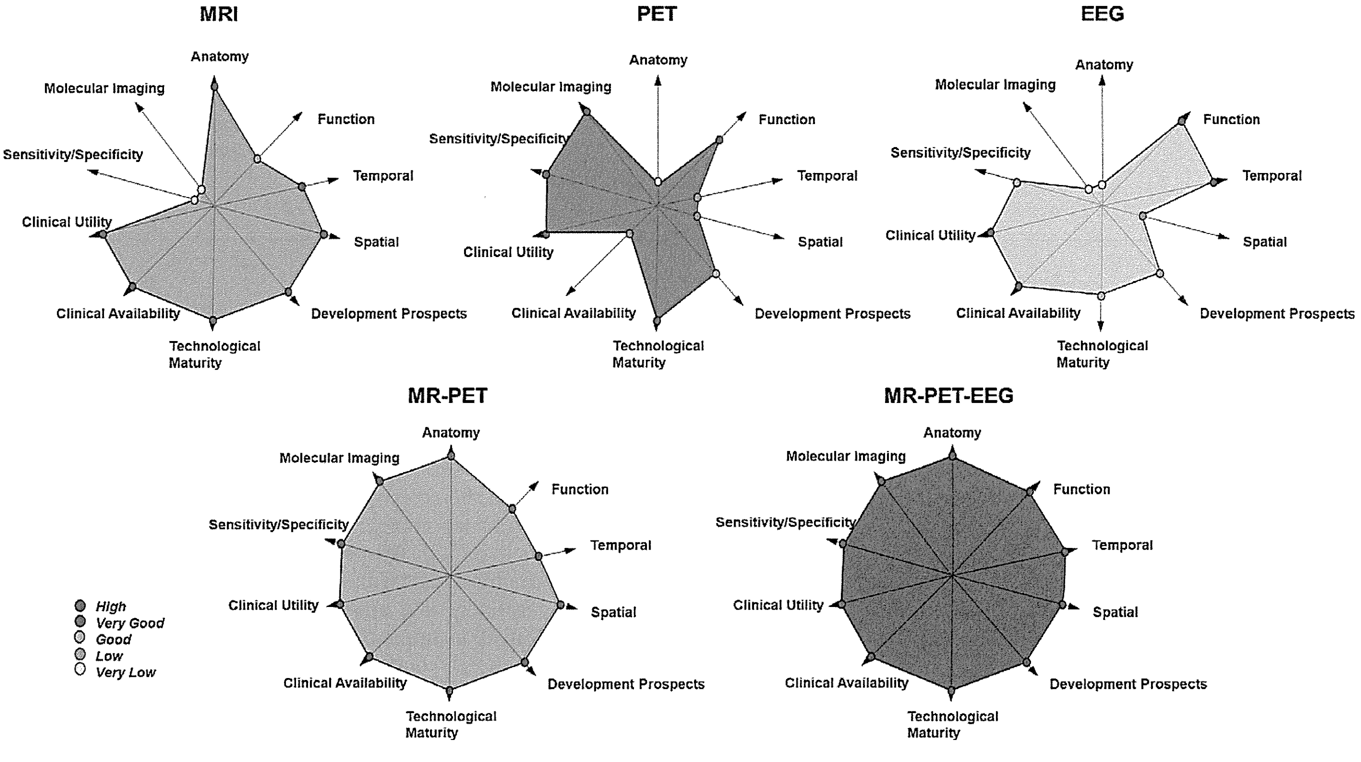

Fig. 1. Fingerprint diagrams giving an overview of the strengths of MRI, PET and hybrid MR–PET, and hybrid MR–PET–EEG. Starting at the origin, the further one traverses along a given axis, the better that particular attribute is fulfilled. MRI can provide exquisite spatial resolution and the technology is widely available. However, MRI is not strong in the area of molecular imaging and its specificity is also somewhat limited. PET on the other hand, has poorer spatial and temporal resolution than MRI but it is extremely specific – an attribute conferred upon it by the choice of radiolabelled tracer – and is also very sensitive. Both MRI and PET have a poor temporal resolution regarding mapping of brain function, for example. In a hybrid scanner capable of simultaneous measurement of all three dataset, all the chosen attributes are fulfilled in entirety.

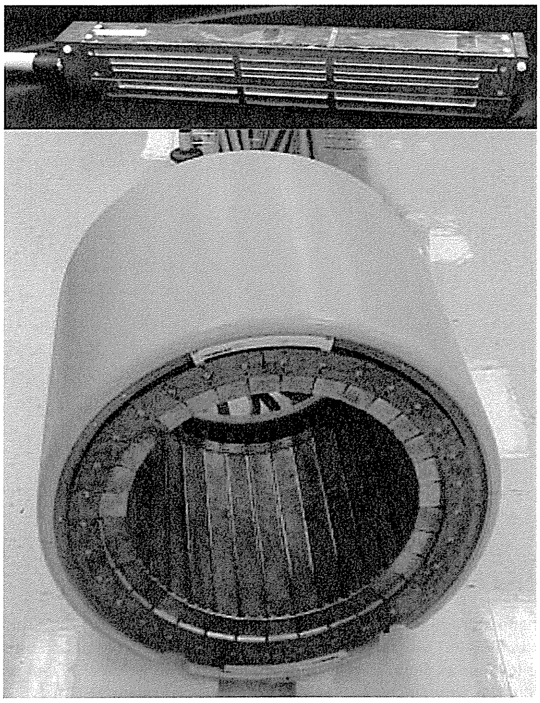

Fig. 2. A view of the interior of the BrainPET insert constructed as a ring of 32 individual cassettes. The BrainPET insert fits into the bore of the magnet of the MRI scanner and is positioned at the isocentre. Each cassette contains six detector modules in a row with a total length of 19.2 cm located towards the front end of the cylinder. Each cassette is individually radiofrequency shielded with a thin copper coating; this is to prevent RF noise generated by the PET electronics from disturbing the MRI signal and to reduce the influence of the MRI-related RF and gradient pulses on the PET system. The cassettes are connected to the MR filter plate by a 10 m, double-shielded cable.

human brain imaging with PET. The inner diameter of the BrainPET is 36 cm, this being the space for the MR head coil. For functional MRI, a custom-built mirror system is clipped onto the receive coil of the MR-head coil which allows for visual stimulus presentation. Hybrid MR–PET systems based on the above insert became available in late 2006 at 3 T and have enabled the acquisition of simultaneously acquired MR–PET data [10–12] some of which are presented below.

2.1. Multimodal imaging – hybrid MR–PET

As noted already, for the diagnostic evaluation of brain tumours, structural MRI is the routine approach. To overcome a challenging task for MRI, additional information from PET in cerebral gliomas, for example, may be very helpful in differentiating between tumour tissue, oedema and post-therapeutic changes in neighbouring tissue. Employing PET with amino acid tracers such as ^{18}F-Fluoroethyl-L-tyrosine (FET) or ^{11}C-L-methionine (MET) has been shown to be a powerful tool to resolve the diagnostic shortcomings of standard MRI examinations [1,13]. It should nevertheless be noted that although it does not form part of a standard examination, use of 1H-MRSI can also add valuable information [14]. Elevated concentrations of the cell membrane marker choline, for example, would support the presence of a tumour whereas a low choline peak in combination with high concentrations of the neuronal marker N-acetyl aspartate (NAA) would rather indicate an inflammatory process [15]. In brain tumours, especially in glioblastoma multiforme and anaplastic astrocytoma, the intracranial mass may be heterogeneous and consist of multiple compartments with differing degrees of malignancy. MRS is of help in the guidance of biopsies in inhomogeneous gliomas of WHO grade IV and also in low grade gliomas that show negative or nonspecific MET uptake with PET [16]. During therapeutic follow-up, amino acid PET and MRSI appear to be helpful in disentangling oedema, necrosis due to radiation therapy and the recurrence of tumour growth.

Diffusion tensor imaging (DTI) can contribute valuable diagnostic information regarding the involvement of white matter and fibre tracts [13,17,18]. Fibre tracking based on DTI data provides spatial information on the impairment of vital white matter fibre tracts, such as the pyramidal tract, by the tumour mass. Tumour infiltration or dislocation of such fibre tracts may considerably influence neurosurgical planning; a hybrid MR–PET examination that includes DTI is of considerable importance in this regard. Further, planning of neurosurgical intervention can be influenced by fMRI to identify eloquent brain areas close to the tumour and its resection zone. The joint findings from a hybrid MR–PET imaging session will impact considerably on the decision reached by the neurosurgeon regarding the necessary aggressiveness/extent of the neurosurgery, the approach to be taken e.g. anterior versus posterior, and the option of awake craniotomy with the possibility of direct cortical stimulation versus resection under general anaesthesia.

2.2. Clinical and neuroscientific applications of MR–PET at 3 T

Metabolic imaging for the differential diagnosis of brain tumours can benefit enormously from the intrinsic temporal and spatial co-registration of MR and PET data acquired in hybrid MR–PET systems [7–9]. Additionally, in the case of heterogeneous brain tumours or for differentiation between active tumour mass and scar tissue after radiation therapy, MR spectroscopy may help to cross-validate and/or extend the PET data. As already noted, the hybrid approach reduces measurement time and greatly aids patient compliance; some patients are simply unable to undergo two separate scans. The feasibility of combining anatomical information from an MP-RAGE acquisition, metabolite-specific information from MR spectroscopy, and FET-PET in the investigation of brain tumours in humans using a hybrid MR–PET scanner was recently demonstrated [12].

MR–PET data from a representative patient from our study comprising a collective of over 50 tumour patients are shown in Fig. 3. The top row of Fig. 3 shows the diffusion parameter FA superimposed on a T_1-weighed MP-RAGE dataset; the crosshairs mark the location of the tumour as determined from FET-PET which shows almost no enhanced tracer uptake in the regions depicted by MRI that are hypointense in the MP-RAGE acquisition. The bottom row of Fig. 3 shows the location of the tumour as well as activation of default mode networks from resting-state fMRI.

MR spectroscopy may also provide metabolic information in addition to FET-PET and detect regional abnormalities of choline, creatine and myo-inositol concentration in large homogeneous low grade gliomas (Fig. 4). This may be an early sign of malignant transformation of a low grade glioma.

These measurements have shown that the acquisition of multimodal MR–PET data sets can contribute significantly to the differential diagnosis of pathological brain lesions. Based on the MR images, the pathological region can be further evaluated by FET-PET and MR-spectroscopy. In cross validation, both image modalities show that the lesion depicted in the MR images (Fig. 4) could be due to inflammation rather than being a malignant tumour thereby illustrating the benefits of multi-modal imaging.

Localisation of functional areas in presurgical fMRI is also an application that benefits from hybrid MR–PET. The appropriate choice of therapy for a brain tumour mandates that the diagnosis encompass the anatomical location, size, spread to different anatomical compartments, and evaluation of tumour malignancy.

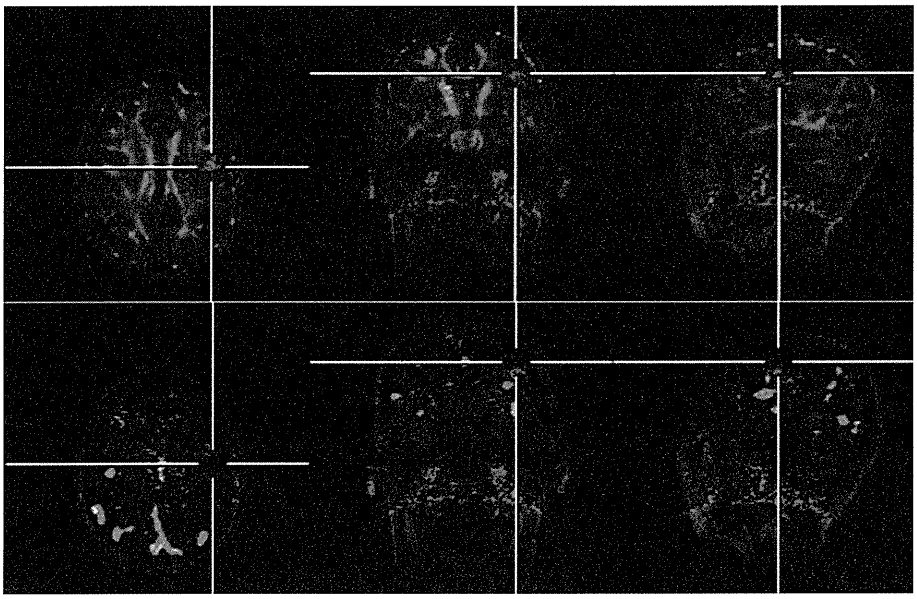

Fig. 3. Images acquired on a hybrid MR–PET scanner comprising a 3 T MAGNETOM Tim-Trio MR and a BrainPET insert. Top: the diffusion parameter, FA, superimposed on a T_1-weigthed MP-RAGE dataset; the crosshairs mark the location of the tumour as determined from FET-PET which shows almost no enhanced tracer uptake in the regions depicted by MRI that are hypointensive in the MP-RAGE acquisition. Bottom: the location of the tumour as well as activation of default mode networks from resting-state fMRI are depicted. PET images acquired within 45 min scanning time after injection of 200 MBq of the amino acid O-(2-[18F]Fluorethyl)-L-Tyrosin (FET).

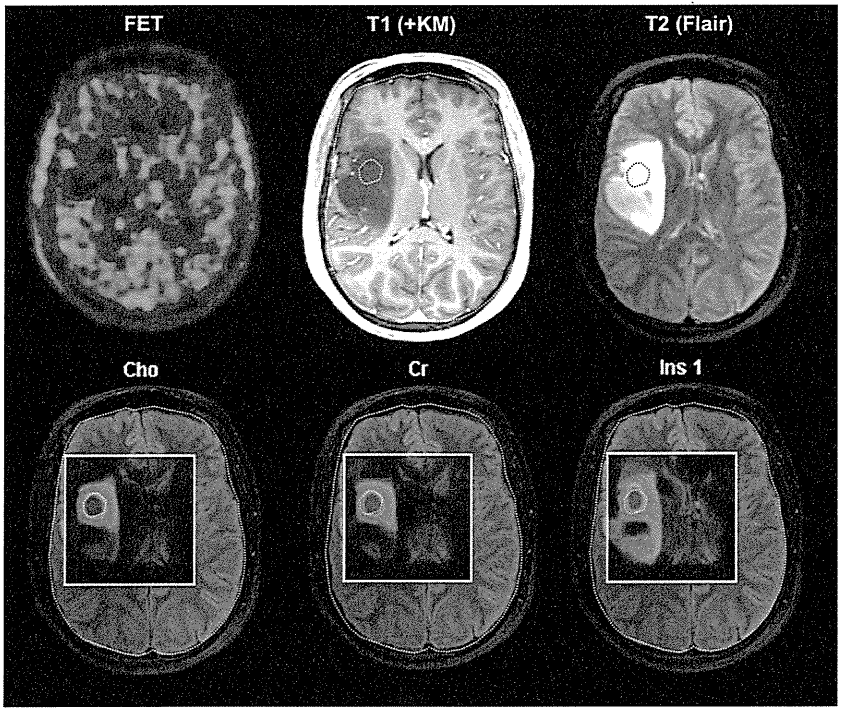

Fig. 4. Patient with a large astrocytoma WHO Grade II in the right temporal lobe. FET PET (upper left) demonstrates low amino acid uptake in the tumour suggesting a favourable prognosis. MRS (chemical shift imaging) shows a regional abnormality in the tumor with increased concentration of choline, creatine and myo-inositol (lower row) which may be an early sign of malignant progression.

Moreover, in contrast to common non-brain tumours, therapy options for these tumours are partially set by their proximity to areas of major brain function, such as motor function, somatosensory, and language, the exact locations of which are dependent upon the individual. Simultaneous MR–PET measurements with optimum temporal and spatial co-registration open up an opportunity to measure the size and the location of the tumour, in relation to regions involving essential brain functions, based on high-resolution MRI and fMRI. Tracer uptake rate, as shown in the PET images, also facilitates insights into the pathophysiology of the tumour, in particular into its degree of malignancy. In Fig. 5, an example of speech area localisation is shown.

The speech area was localised by employing standard, BOLD-based fMRI during stimulation with a speech localisation paradigm comprising a block design of 4 × 36 s stimulation periods nested into five resting periods of 18 s duration each [19]. Briefly, in order

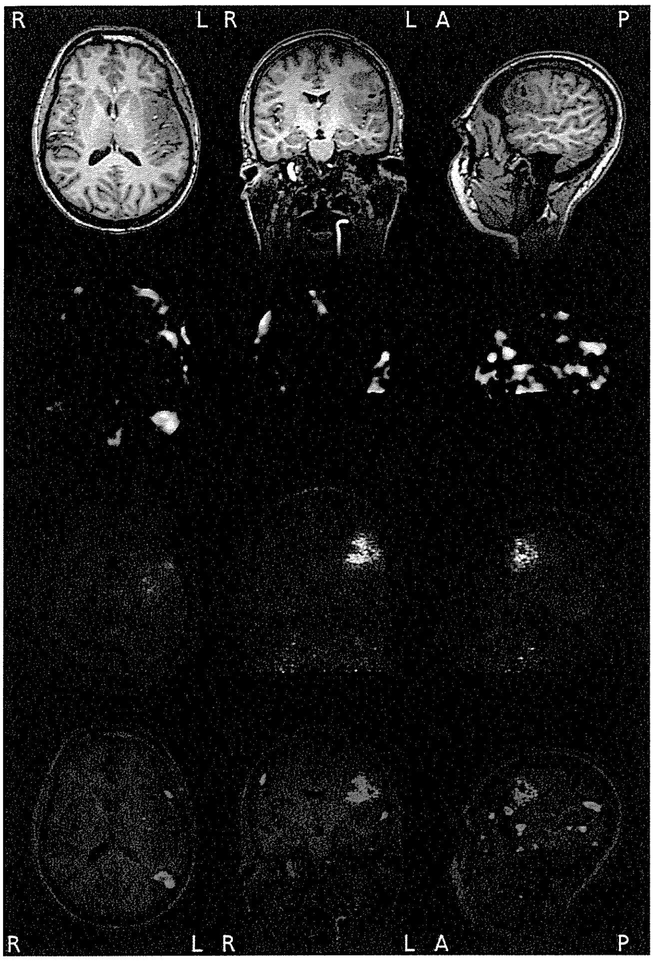

Fig. 5. Data from a 38-year old women suffering from a left, fronto-temporal oligoastrocytoma. Top row: The MRI data from a T_1-weighted MPRAGE sequence (1 mm isotropic resolution) shows an oligoastrocytoma fronto-temporal on the left side. 2nd row: The language localisation paradigm yields a strong BOLD signal at the position of the speech associated areas. 3rd row: The FET-PET reveals a tracer enhancement at the location of the tumour (200 MBq, 50 min scanning time). Bottom row: Fusion of the three imaging modalities; this transverse slice (bottom, left) shows a bright occipito-temporal area of fMRI activation which corresponds to the activation of the Wernicke speech area far from the tumour. On the same slice, it can be seen that the tumour is beginning to infiltrate the Broca language area at its fronto-lateral border. This additional information can guide decisions regarding the appropriate therapy for this patient.

to fully stimulate the complex speech area, the paradigm comprises two parts, word and sentence generation. For word generation, generic terms were presented on a display and the patient was required to find matching examples. In the sentence generation paradigm, simple pictures were presented which had to be transferred into sentences.

The data from a 38-year old woman suffering from a left, fronto-temporal oligoastrocytoma are shown in Fig. 5. The transverse slice (bottom, left) shows a bright occipito-temporal area of fMRI activation which corresponds to the activation of the Wernicke speech area far from the tumour. On the same slice, it can be seen that the tumour is beginning to infiltrate the Broca language area at its fronto-lateral border. This additional information can guide decisions regarding the appropriate therapy for this patient.

2.3. Multimodal imaging – simultaneous fMRI–EEG at 3 T

Functional MRI, relying on the measurement of the BOLD effect, has successfully been used to probe functional aspects of the brain including the assessment of different sensory, cognitive, emotional and social tasks [20,21]. However, the main drawback of fMRI is the fact that the BOLD effect is an indirect measure of brain function with a low temporal resolution due to the delayed haemodynamic response. This restriction can be overcome by the simultaneous measurement of fMRI and electrophysiology [22–24]. Electrophysiological measures (e.g. EMG and EEG) assess neuronal function on a millisecond timescale, thus providing the temporal resolution missing in fMRI. fMRI on the other hand provides excellent spatial resolution that is lacking in EEG data. Combining fMRI and EEG measures thus allows one to probe a scientific question in one individual with two modalities spanning a high spatial resolution (MRI/fMRI) and a very fine temporal resolution (EEG) at the same time under exactly the same physiological, psychological and technical conditions. Neuroscientific studies involving paradigms where a parallel paradigm version might evoke confounding factors, studies using pharmacological challenges or paradigms relying on novelty effects also profit from a simultaneous approach due to the elimination of order and learning effects. The simultaneous approach is also important for the investigation of the "resting state" [25,26]. It allows for the analysis of the underlying neuronal phenomena of oscillation amplitude fluctuations in the EEG data which reflect functional states and can be used for the definition of such states. Furthermore, these have been shown to affect behaviour when occurring in a task context. Simultaneous EEG–fMRI has proved to be particularly useful in studies of sleep and epilepsy where significant events, such as epileptic spikes or sleep onset, can be identified in the EEG and used for appropriate analysis of the fMRI data [27]. Without the high temporal resolution EEG data for event identification, effective analysis of the fMRI data would not be possible.

Simultaneously acquired EEG/fMRI data are also a prerequisite for a single trial analysis approach to integrating EEG and fMRI data. Based on the single trial e.g. prepulse–pulse inhibition (PPI) of the startle reflex or P300 latency or amplitude, an electromyography (EMG) or EEG-informed fMRI analysis becomes feasible [22,28–30]. In a classical approach to EEG and fMRI data analysis, averaging of trials is usually performed meaning that the trial-to-trial evoked response variability is averaged out [31]. Fluctuations in evoked responses such as the P300 as well as spontaneous activity changes e.g. during "resting state" investigations mirror fluctuations of an internal and predictive contextual representation [32], thus making this variability meaningful and these data could broaden the functional understanding of neuronal networks.

The examples above show how both modalities complement each other effectively. However, the simultaneous acquisition of fMRI and EEG data is technically challenging and comes at a price with regard to data quality. From a technical perspective recording EEG during fMRI requires an MR-compatible EEG-system (which are commercially available) and great care during recording inside the scanner to ensure safety of the volunteers and acceptable data quality [22,29]. In terms of quality, EEG data acquired simultaneously with fMRI data suffer two types of artefacts: (a) the so-called cardioballistic artefact or pulse related artefact caused by slight pulse-induced head motion and by pulsation of scalp vessels within the magnetic field, and (b) the gradient artefact caused by switching of the gradients during the EPI sequence favoured for fMRI [33]. As shown in Fig. 6, both artefacts can be successfully removed from the EEG by different methods such as Artefact Average Template Subtraction [34], Optimal Basis Set [35] or Independent Component Analysis [36,37]. As MRI moves towards ultra-high field imaging the question of whether the simultaneous approach would still be feasible needs to be addressed. EEG data acquired at 7 T [36] and 9.4 T [38] show that the cardiac-related pulse artefact increases linearly with field strength and is more challenging to remove from the data, but that in principle EEG

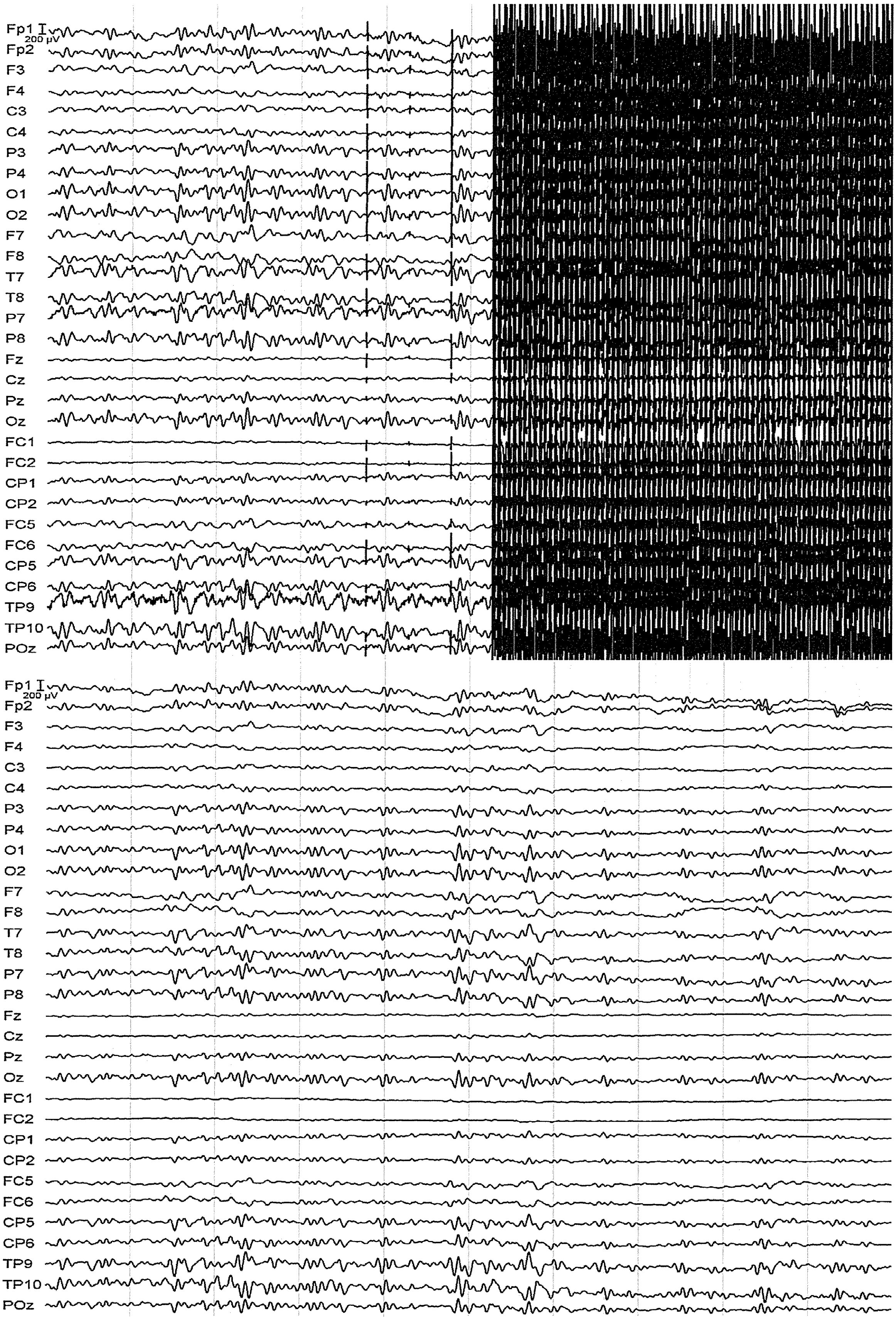

Fig. 6. The upper part of the figure shows uncorrected EEG-data acquired in a 3 T MR scanner: The left side shows data prior to the start of the MRI acquisition, distortion due to the cardio-ballistic artefact in the static field can be seen. The right side of the image shows the gradient artefact. The lower part of the figure shows the same section of data that has been corrected for cardio-ballistic artefact and gradient artefact.